

Electronic Transport Properties in Single-layer CVD graphene

by

Mai Sakuragi

A thesis
presented to the University of Waterloo
in fulfillment of the
thesis requirement for the degree of
Master of Science
in
Physics

Waterloo, Ontario, Canada, 2022

© Mai Sakuragi 2022

Author's Declaration

I hereby declare that I am the sole author of this thesis. This is a true copy of the thesis, including any required final revisions, as accepted by my examiners.

I understand that my thesis may be made electronically available to the public.

Abstract

Graphene is a two-dimensional material of carbon atoms possessing a metallic nature and the low-energy quasiparticles behave as massless Dirac fermions. The unique electronic properties of graphene inspire many researches in fundamental physics, and its extraordinary mechanical strength and high thermal and electrical conductivity make graphene as potential material in the nano-electronic devices. The chemical vapor deposition (CVD) has enabled a large scale growth of graphene, and the applications such as magnetic field sensors and tunnelling transistors rely on the scalable fabrication techniques. However, charge carrier mobilities of CVD graphene reported so far are still relatively lower than exfoliated graphene due to the conventional wet-transfer method, and the state of the art technique to overcome this is the dry transfer or the encapsulation of graphene with hexagonal boron nitride (hBN).

This thesis presents an experimental study of electronic transport properties in single-layer graphene. Hall bars are fabricated with 1cm^2 -sized commercial CVD graphene using photolithography and O_2 plasma etching. The electric field effect and the Dirac point in graphene are characterized by applying an external gate voltage, and the magnetotransport in graphene is measured. The gate-voltage dependence on the weak-localization in the measured magnetoresistance is studied. Graphene samples are *in-situ* annealed with high current density to remove the impurities on graphene surface and its effect on the electronic transport is studied. Lastly, the resistance in Ni/Au and Pd contacts is compared.

Acknowledgements

I would like to thank my supervisors Dr. Jonathan Baugh and Dr. Na Young Kim for all of your support during the Master's program here at the University of Waterloo, and for providing me with great opportunities and resources to get involved in interesting experimental physics research. I am thankful to my supervisors for their patience and for encouraging me not to give up and keep going when I was having a hard time through COVID. The research work presented in this thesis would not have become possible without your support. I thank the members of my examination committee Dr. Raffi Budakian, Dr. Robert Hill, and Dr. Anton Burkov for your feedback on my research and thesis.

I would also like to thank the clean room staff at the Quantum Nano-Fabrication and Characterization Facility for their assistance in the fabrication and for providing the members with well-administered work environment. I am grateful for them for always making sure the tools are available to use.

I thank Dr. François Sfigakis for teaching me sample characterizations and helping me build the fabrication process recipes. It would not have been possible to fabricate working devices without your help and I owe a big thank you for the entire work in this thesis. Thank you for working with me on late night measurements.

I would like to thank the group members in our lab for their advice on research and coursework and being a support. Lastly, I want to thank all of the people I met in IQC and in the cleanroom for the socializing time.

Dedication

This is dedicated to the one I love.

Table of Contents

List of Figures	viii
List of Tables	x
1 Introduction	1
1.1 Background	1
1.1.1 Crystal structure of graphene	1
1.1.2 Electronic band structure of graphene	2
1.2 Motivation	5
1.2.1 Graphene based nano-electronic quantum device	5
1.2.2 Quantum Hall effect in graphene	9
2 Fabrication	14
2.1 Geometry of graphene Hall bars	14
2.2 Fabrication process of Hall bars	16
3 Characterization	19
3.1 Contacting back-gate	19
3.2 Transport properties of graphene	19
3.2.1 Magneto-transport in graphene	20
3.2.2 Electronic mobility and density	25

3.2.3	Dependence of resistance on gate voltage	29
3.2.4	Disorder and weak localization in graphene	31
3.3	Ni/Au and Pd Ohmic contacts	33
4	Current annealing of graphene	36
4.1	Dirac point shift	38
4.1.1	Doping of graphene	38
5	Conclusions	42
	References	44
	APPENDICES	50
A	Device Fabrication	51
A.1	Fabrication recipes	51

List of Figures

1.1	The honeycomb lattice and the reciprocal lattice of graphene	2
1.2	Band structure of graphene and the first Brillouin zone	3
1.3	Shubnikov-de Haas oscillations and conductivity minimum in graphene . .	11
1.4	Shubnikov-de Haas oscillations and QHE	11
2.1	Geometry of graphene Hall bars	15
2.2	Chip design	16
2.3	SEM image of a Hall bar	18
3.1	Magnetoresistance and Hall resistance as a function of back gate voltage .	22
3.2	Magnetotransport	23
3.3	Magnetoresistance	24
3.4	Magnetoresistance	25
3.5	Density dependence on back gate voltage	27
3.6	Density dependence on back gate voltage	28
3.7	Mobility vs back gate voltage	29
3.8	Four-terminal resistance as a function of back gate voltage at $B = 0V$	31
3.9	Weak localization in graphene at different gate voltages	33
3.10	Contact resistance	35
4.1	Annealing current as a function of time	38
4.2	Resistance of graphene measured at RT and 1.64K before and after annealing	40

4.3	Change in the resistance of graphene before and after annealing	41
A.1	Optical micrograph of graphene channel after step 2(d) of section 2.2 . . .	55
A.2	Optical micrograph of graphene Hall bar without pre-baking.	55

List of Tables

3.1	Dimension and metals used for electrodes in the characterized samples . . .	20
-----	---	----

Chapter 1

Introduction

1.1 Background

1.1.1 Crystal structure of graphene

Graphene is a 2-dimensional structure of carbon atoms arranged in a honeycomb lattice. The lattice structure of graphene is composed of triangular Bravais lattice with basis vectors (\mathbf{a}_1 , \mathbf{a}_2), and each unit cell has two atoms. The basis vectors are described as follows:

$$\mathbf{a}_1 = a \left(\frac{\sqrt{3}}{2}, \frac{1}{2} \right), \quad \mathbf{a}_2 = a \left(\frac{\sqrt{3}}{2}, -\frac{1}{2} \right) \quad (1.1)$$

where $a = \sqrt{3}a_0$ and $a_0 = 1.42\text{\AA}$ representing the distance between nearest neighbours. The reciprocal lattice vectors (\mathbf{b}_1 , \mathbf{b}_2) are defined as $\mathbf{a}_i \cdot \mathbf{b}_j = 2\pi\delta_{ij}$, and this gives

$$\mathbf{b}_1 = b \left(\frac{1}{2}, \frac{\sqrt{3}}{2} \right), \quad \mathbf{b}_2 = b \left(\frac{1}{2}, -\frac{\sqrt{3}}{2} \right) \quad (1.2)$$

where $b = 4\pi/a\sqrt{3}$. The basis vectors of the Bravais lattice and reciprocal lattice are shown in Fig.1.1. The Brillouin zone of graphene is hexagonal-shaped, and the wave numbers of the two of its six corners are non-equivalent since others can be expressed as the sum of either of the two and a reciprocal lattice vector. Those two wave numbers are denoted as \mathbf{K}_- and \mathbf{K}_+ as shown in Fig.1.1, and the six corners are referred to as the Dirac points. There are two other types of highly-symmetrical points in the first Brillouin zone (FBZ),

denoted as Γ , which is located at the center of the FBZ, and \mathbf{M} , which is located at the midpoint of \mathbf{K}_- and \mathbf{K}_+ . Therefore, there are three \mathbf{K}_- and \mathbf{K}_+ points, and six \mathbf{M} points in the FBZ. These points are described as follows [1]:

$$\mathbf{K}_+ = \frac{4\pi}{3a} \left(\frac{\sqrt{3}}{2}, -\frac{1}{2} \right), \quad \mathbf{K}_- = \frac{4\pi}{3a} \left(\frac{\sqrt{3}}{2}, \frac{1}{2} \right), \quad \mathbf{M} = \frac{2\pi}{\sqrt{3}a} (1, 0). \quad (1.3)$$

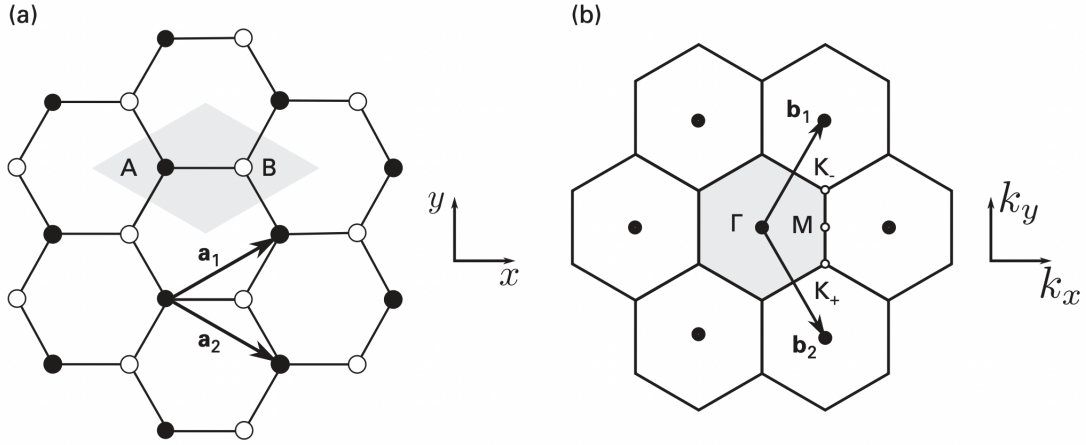


Figure 1.1: **The honeycomb lattice (a) and the reciprocal lattice (b) of graphene.** (a) The primitive unit vectors \mathbf{a}_1 and \mathbf{a}_2 and the triangular Bravais lattice with a basis of atom A (solid) and B (empty). (b) The reciprocal lattice vectors \mathbf{b}_1 and \mathbf{b}_2 with two non-equivalent points \mathbf{K}_- and \mathbf{K}_+ and other high-symmetry points Γ and \mathbf{M} of the FBZ. The primitive unit cell and the FBZ are shown shaded gray [1].

1.1.2 Electronic band structure of graphene

The band structure of solids is found by solving the time-independent Schrödinger's equation

$$H\Psi(k, r) = E(k)\Psi(k, r) \quad (1.4)$$

where H is the Hamiltonian for an electron in a periodic crystal structure that operates on the wavefunction Ψ , and is given by

$$H = \frac{\hbar^2 \nabla^2}{2m} + \sum_i V(\mathbf{r} - \mathbf{R}_i). \quad (1.5)$$

Here, \mathbf{R}_i represents the position of the i th atom in the Bravais lattice. In periodic systems, potential energy satisfies the relation $V(\mathbf{r} + \mathbf{t}) = V(\mathbf{r})$ for all \mathbf{t} which is any linear combination of the primitive vectors ($\mathbf{a}_1, \mathbf{a}_2$). The wavefunction here satisfies the Bloch's theorem which states that the wavefunction of an atom at position \mathbf{R}_i differs from that of an atom at \mathbf{R}_j by a phase of $e^{i\mathbf{k} \cdot (\mathbf{R}_i - \mathbf{R}_j)}$, and therefore can be described as follows:

$$\Psi(\mathbf{r} + \mathbf{R}) = e^{i\mathbf{k} \cdot \mathbf{R}} \Psi(\mathbf{r}). \quad (1.6)$$

The electronic structure of graphene is generally described by the nearest-neighbor tight-binding model, where the *ansatz* for the wavefunction is generally a linear combination of two Bloch functions, with each representing one of the two atoms in the unit cell. The detailed calculation of the solution to eq.1.4 will be omitted in this thesis. Solving for eq.1.4 involves a diagonalization of a 2×2 Hamiltonian, and one obtains

$$E(k_x, k_y) = \pm \gamma \sqrt{1 + 4 \cos \frac{\sqrt{3}k_x a}{2} \cos \frac{k_y a}{2} + 4 \cos^2 \frac{k_y a}{2}} \quad (1.7)$$

where $\gamma \approx -2.7\text{eV}$ is the hopping parameter [2, 3].

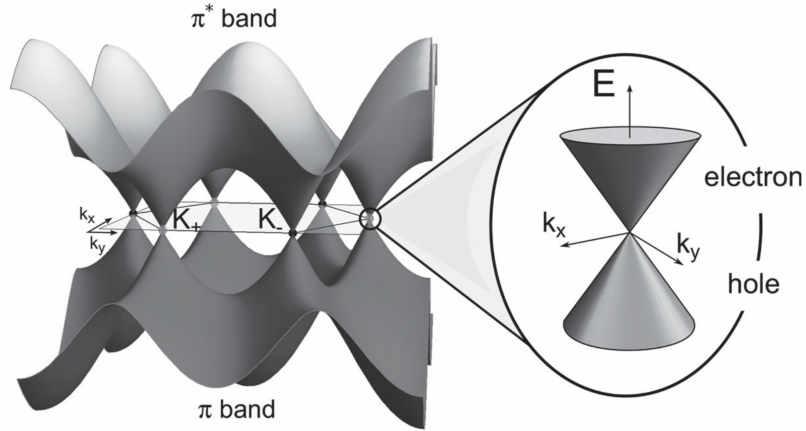


Figure 1.2: **Band structure of graphene and the first Brillouin zone.** Localized bonding (π) and the anti-bonding (π^*) orbitals of graphene electronic band structure [1]. Dirac cone is shown on the right.

Fig.1.2 shows the dispersion of graphene throughout the FBZ with conduction (π^*) band in the positive $E(k_x, k_y)$ and valence (π) band in the negative side. In graphene, the

conduction band and the valence band cross at the charge neutrality points (CNPs), and the Fermi level is located at the CNP in undoped graphene. Thus, there is no bandgap at the Fermi level (E_F), and graphene is metallic in nature. The Fermi surface consists of the \mathbf{K}_- and \mathbf{K}_+ points which form a zero dimensional finite set of points, and thus, graphene is termed semi-metal.

By approximating the Hamiltonian around \mathbf{K}_- and \mathbf{K}_+ by linear expansion, we can obtain an effective Hamiltonian as follows:

$$H_{\mathbf{K}_+} = \hbar v_F \begin{pmatrix} 0 & k_x - ik_y \\ k_x + ik_y & 0 \end{pmatrix} = v_F(p_x \sigma_x + p_y \sigma_y) \quad (1.8)$$

where $p = \hbar k$ is the momentum, v_F is the Fermi velocity, and σ_i are the Pauli matrices. The eq.1.8 can be written in another way as follows:

$$H_{\mathbf{K}_+} = v_F \boldsymbol{\sigma} \cdot \mathbf{p}. \quad (1.9)$$

The other non-equivalent point is given by transposing this Hamiltonian as $H_{\mathbf{K}_-} = H_{\mathbf{K}_+}^T$. The Pauli matrices in eq.1.9 operate on the spatial degree of freedom instead of real spin because of the sublattice with two carbon atoms per unit cell. Thus, $\boldsymbol{\sigma}$ is termed pseudospin [3]. Substituting $\hat{\mathbf{p}} = -i\hbar\nabla$ in eq.1.9 results in the Hamiltonian given by the Dirac equation by setting the particle rest mass to zero in quantum electrodynamics [1]. Diagonalizing eq.1.9 gives the spectrum $E(\mathbf{k}) = \pm v_F \hbar k$, where the value of Fermi velocity has been shown experimentally as $v_F = 3\gamma a_0/2\hbar \approx 1.1 \times 10^6 \text{ m/s}$ [4, 5]. Thus, the solution of 2D massless Dirac equation gives a linear dispersion relation near Dirac points, and the electronic transport in graphene within low-energy excitations is described by the Dirac equation for massless Fermions. The corresponding quasiparticles are thus often referred to as massless Dirac fermions. The charge carriers behave like relativistic particles with zero effective mass and velocity v_F . Thus, electronic properties of graphene are governed by the quantum electrodynamics rather than the Schrödinger-equation based standard physics [6]. The linear region of the dispersion relation is generally referred to as the "Dirac cones" in its 3D plot. The linear dispersion has been shown to be up to about $\pm 0.6 \text{ eV}$ by experimental results [7]. This unique band structure of graphene leads to some novel transport properties such as ambipolar field effect, weak localization, and conductivity minimum, which can not be seen in conventional materials. The density of states $\rho(E)$ per spin and per unit cell is $\rho(E) = dN(E)/dE$, and using the relation $N(E) = 3\sqrt{3}a_0^2 E^2/4\pi v_F^2 \hbar^2$ gives $\rho(E) = 2|E|/\pi\sqrt{3}\gamma^2$. Density of states in graphene is linearly dependent on energy. In undoped graphene, Fermi energy is at the Dirac point and is zero. Thus, density of states vanishes at the Dirac point.

The charge carrier mobility denoted as μ is defined as the proportionality constant that defines the drift velocity v_d of carriers as $v_d = \mu E$, where E is the electric field strength, and is written in the units of $\text{cm}^2 \text{ V}^{-1} \text{ s}^{-1}$ [8]. The carrier mobility is therefore an useful parameter that determines the average scattering of carriers as they travel inside the solid or the extent of disorder in the system [2]. In experimental studies, μ is generally associated with semiclassical conductivity σ_{sc} that is a linear function of $\rho(E)$ in the diffusive regime, and is given by

$$\mu(E) = \frac{\sigma_{\text{sc}}}{n(E)e} \quad (1.10)$$

where $n(E) = \int dE \rho(E)$ is the carrier density and e is the elementary charge [1]. This is the Drude model. Since mobility is determined by the scattering inside a material, it can be also related to the mean free path λ , which is the average distance an electron travels before being scattered. Therefore, mobility can also be expressed as $\mu = e\tau/m^* = e\lambda/\sqrt{3k_{\text{B}}Tm^*}$ where m^* is the effective mass, k_{B} is the Boltzmann constant, T is the absolute temperature, and τ is the mean free time.

1.2 Motivation

1.2.1 Graphene based nano-electronic quantum device

Ever since graphene was first discovered by A.K.Geim in 2004 by succeeding to exfoliate a 2D material from graphite with a scotch tape on a SiO_2 substrate [9], graphene has attracted many interests, and its electronic transport and optical properties have been actively studied. The highest mobility reported on graphene so far is $350,000 \text{ cm}^2 \text{ V}^{-1} \text{ s}^{-1}$ measured at 1.6K from chemical vapor deposition (CVD)-grown graphene which is transferred while avoiding any contact with chemicals that cause contamination of graphene in a conventional "wet" transfer method. The transfer method uses the van der Waals forces between hexagonal boron nitride (hBN) and graphene. An hBN flake on a stack of different kinds of polymers are used to pick up graphene that has been grown on copper (Cu) with CVD, and to make a hBN/graphene heterostructure [10]. This transfer method is classified as "dry", as opposed to wet transfer methods which have been used for most of CVD-grown graphene simply due to the simplicity and scalability [11].

CVD is a technique to deposit thin film on substrates through chemical reactions or decomposition using the vapor species. Reactive hydrocarbon gas species are supplied into the reactor as precursors for graphene growth, and chemical reactions and solid deposition take place in the reactor that is surrounded by heaters which provide high temperatures

required for the reactions. Generally, these reactions are associated with by-products which are then removed by the gas flow inside the system. Quartz tubes with a diameter of $\sim 8\text{cm}$ is typically used as a reactor where growth typically occurs at around $800\text{-}1000^\circ\text{C}$ [1, 10, 12, 13]. Precursors for graphene growth are typically a mixture of methane and hydrogen, of which the flow rates are controlled. Graphene growth involves the use of catalyst foils, which are generally copper or germanium, to lower the energy barrier of the reaction because high energy barrier is not desirable for controlling the quality of deposited films. Different metals have different carbon solubility, and the growth mechanism of graphene depends on the solubility [14]. CVD allows a mass-production of graphene, and therefore it is a desired growth method for future graphene electronics. However, large scale production of graphene makes polycrystallinity unavoidable. This polycrystallinity causes the topological defects such as dislocations and grain boundaries where domains of different sizes intersect and stitch together. The presence of grain boundaries is considered to significantly degrade the mechanical strength of graphene, whereas its electrical properties are not so drastically modified [1].

CVD enables wafer-scale growth of single-layer graphene [12, 13, 15], while exfoliated graphene flakes can only be up to a size of $\sim 100\mu\text{m}^2$, and thinner graphene flakes such as monolayer graphene is generally more challenging to obtain in a large scale. Exfoliation is therefore not a scalable and efficient growth technique for graphene nano-electronic device fabrication. CVD growth, however, can also bring a critical bottleneck in graphene device fabrication since mobility of CVD-grown graphene is typically limited by the conventional wet transfer techniques, and it is significantly lower ($\mu < 3000\text{ cm}^2\text{ V}^{-1}\text{s}^{-1}$) than what has been achieved by exfoliated graphene devices [10]. This is mainly due to scattering from charged impurities and defects that are generated during the transfer process of graphene from the growth substrate such as copper and germanium onto an insulating substrate such as SiO_2 [16]. Poly methyl methacrylate (PMMA) is commonly used as a polymer which supports graphene while copper substrate is chemically etched away, and PMMA is spin-coated directly on graphene. This wet transfer method creates chemical residues which significantly degrades the electronic properties of graphene and results in a mobility drastically reduced from pristine graphene [10].

In 2019, De Fazio *et al.* reported a mobility of $\sim 120,000\text{ cm}^2\text{ V}^{-1}\text{s}^{-1}$ at 9K in a CVD-grown graphene Hall bars which use the common wet transfer method and the encapsulation with hBN layers. Single crystal monolayer graphene is grown by CVD on Cu. PMMA is spin-coated on graphene on Cu, and the sample is put into a solution of ammonium persulfate and deionized (DI) water to chemically etch Cu. The PMMA/graphene stack is moved into DI water to remove residual ammonium persulfate, and then picked up with SiO_2/Si substrate. PMMA is removed with acetone. The hBN layers are exfoliated

flakes, and the encapsulation is performed using a stamp of polycarbonate (PC) film on polydimethylsiloxane (PDMS) where PDMS serves as a mechanical support. The hBN flake on a SiO_2/Si substrate is transferred using a heated stage with different temperatures at each step of the transfer process. The use of heat at $\sim 180^\circ\text{C}$ is for the transfer purpose with polymers itself as well as for removing the adsorbates trapped between hBN flakes and graphene. Combining the interface thermal cleaning and encapsulation enabled relatively high mobility even using the conventional wet transfer technique [11].

Due to its excellent electric and thermal conductivity, graphene is a potential candidate for next-generation material for nanoelectronic devices, and the relativistic nature of carriers in graphene attracts fundamental study of physics. Some applications in electronic devices include Hall sensors [17, 18], field-effect transistors [19], quantum dots [20], and nanoribbons [21]. In 2018, Cao *et al.* showed an unconventional superconductivity in bilayer graphene in which one layer is twisted at a certain angle from the other. They found that at the twist angle of $\theta = 1.1^\circ$, v_F goes to zero and the electronic band structure of the bilayer graphene becomes flat near CNPs, resulting in a high effective mass in the flat energy band region and correlated insulating states. Superconductivity is shown within $E_F < 0$ as their bilayer graphene Hall bar is doped away from the insulating state by applying a gate voltage, and critical temperature up to 1.7K. The demonstrated tunable properties of their bilayer graphene device to be either in insulating, metallic, or superconducting state is remarkable. Finding such advantage is useful in fabricating quantum electronic devices because they generally require many different materials with multiple fabrication steps, which could cause material incompatibilities [22]. Rodan-Legrain *et al.* further studied the tunable characteristics of twisted bilayer graphene and demonstrated the Josephson junctions as a potential application of graphene van der Waals heterostructure into superconducting circuits. By patterning top gates differently on two different types of devices, they fabricated multi-gated devices that are used to demonstrate multiple functionalities of hBN-twisted bilayer graphene-hBN heterostructure. In one of their devices, the top-gate voltage controls the semiconducting weak link between superconducting electrodes and forms a junction that turns the electronic state of the device from insulating to metallic to superconducting phases. Their other devices have two isolated top gates with a $\sim 100\text{nm}$ gap in between to form a p-n junction where half of the device is brought into a superconducting state, and the other half is brought into a normal metallic state. When current passes through the gap, the carrier density reaches an insulating regime, and a tunnelling spectroscopy into the superconducting regime is formed. By creating a single-electron transistor with the same device geometry with p-n junction, they also explored the Coulomb blockade in the twisted bilayer graphene [23].

Wang *et al.* studied the Andreev Reflections in superconductor/graphene (SC/g) junc-

tions under large magnetic fields. Andreev Reflection (AR) occurs when an electron that is incident on the interface between a normal metal and a superconductor transitions into the superconductor, but the incident electron has a smaller energy than the superconducting energy gap. At the interface, a Cooper pair is formed in the superconductor, and a hole with an opposite spin from the incident electron is retro-reflected in the normal metal. The probability for the AR to occur depends on the properties of the interface and the band structure of the normal metal. Their initial work in 2016 identified two different cases of AR. One is the normal AR where the hole is reflected along the same path as the incident electron. In a typical normal metal, E_F is substantially larger than a superconducting gap. However, with a low-disordered graphene, it is possible to tune E_F to be smaller than the superconducting energy gap. In the other case of AR they discovered, the reflection of hole becomes specular at the interface for this energy limit [24]. Wang *et al.* investigated the effect of varying the E_F of graphene and the DC bias current on the AR under zero, perpendicular, and parallel magnetic fields, and showed a change in the response of junction conductance. To achieve a low-disordered SC/g junction, they fabricated a niobium nitride (NbN)/graphene interface with a low resistance by edge-contacting graphene, and bilayer graphene is encapsulated by top and bottom hBN to form a heterostructure [25].

The valleytronics applications or the implementation of valley degree of freedom of graphene into electronic devices have also been explored [26, 27]. Graphene has two degenerate valleys at the \mathbf{K}_- and \mathbf{K}_+ points in the FBZ [26, 28], and the band structure of monolayer graphene has a finite Berry phase [29]. When graphene is aligned on top of hBN with an angle near 0° , a Moiré pattern appears due to their lattice mismatch, and the spatial inversion symmetry breaks. As a result, a bandgap is created at the Dirac points of the two valleys, and the Berry curvature is induced. Modification in band structure generates "hot spots" near the bandgap at the apex of Dirac cone where non-local response is exhibited when graphene E_F is tuned into those spots [30]. These effects are important factors that determine the transport properties of graphene [29, 30]. In valleytronics, valley degree of freedom has been controlled magnetically, electrically, or optically, and the Berry curvature in graphene allows an electrical control [26]. The topological currents generated by the applied electric field have opposite signs at \mathbf{K}_- and \mathbf{K}_+ points [29], which then induce the valley Hall effect. Because these valleys are largely separated in momentum space, the intervalley scattering is weak enough so that the total topological currents can be long-range and neutral in charge [28]. Furthermore, the bulk topological current can be induced at $B = 0$ and without breaking the time-reversal symmetry. Gorbachev *et al.* observed topological currents in graphene/hBN superlattice through measuring the non-local resistance (R_{nl}) which exhibits one sharp peak at the back-gate voltage of approximately 0V and another minor peak on the hole side. Similar results were observed in Komatsu *et*

al. where they measured the bulk topological currents in ballistic regime, and denoted the two peaks as Dirac point ($V_g \approx 0V$) and the secondary Dirac point. Gorbachev *et al.* and Komatsu *et al.* both observe a similar value for $R_{nl} \sim 1k\Omega$ at the Dirac point. Komatsu *et al.* describes that R_{nl} at the secondary Dirac point is the result of the modification in the band structure due to the hBN aligned to graphene, and its magnitude is approximately $h/2e^2 = 12.9k\Omega$ which is a quantized value. Based on their consistent observation of quantized R_{nl} at $B = 0$ in their superlattice device, they conclude that is the quantum valley Hall state where electrons at the two valleys are separated and flow to the opposite transverse directions under an applied in-plane electric field. This effect is referred to as the edge state [28, 30].

1.2.2 Quantum Hall effect in graphene

The quantum Hall effect (QHE) was first discovered in 1980 by K.v.Klitzing *et al.* when their MOSFET device showed Landau quantization of electron motion under a strong magnetic field in a cold temperature [31]. QHE is a quantized Hall resistance observed in 2D electron systems, where conductance value only takes the multiples of e^2/h where h is the Planck constant, and e is the elementary charge. By definition, the Hall conductivity σ_{xy} is quantized and takes values at $\sigma_{xy} = 2Ne^2/h$ where N here can be either an integer or a fraction ($N = 1/3, 2/5, 3/7, 2/3, 3/5, \dots$). The QHE in graphene was first observed soon after the discovery of graphene in 2004. The half-integer QHE and the Berry's phase were shown with mechanically exfoliated monolayer graphene [32]. The half-integer QHE is a unique feature of monolayer graphene which is not observed in multi-layer graphene, and the Hall conductivity takes values at $\sigma_{xy} = 4e^2/h \times (N + 1/2)$ [1, 5]. QHE in graphene has also been demonstrated at room temperature under a magnetic field of 29T in an exfoliated graphene Hall bar with a mobility of $10,000 \text{ cm}^2\text{V}^{-1}\text{s}^{-1}$ [33]. Owing to its large energy gap in the Landau level spectrum, graphene does not require as low temperatures and high magnetic fields as conventional semiconductors to observe QHE.

Another quantum mechanical effect related to the Landau quantization is Shubnikov-de Haas oscillations (SdHOs) which is an oscillation in the magnetic field dependence of 2-dimensional electron gases (2DEG) resistivity or conductivity in the longitudinal direction. The unique feature of SdHO in graphene is that the longitudinal resistance (ρ_{xx}) shows maxima at integer values of the Landau filling factor ν rather than minima which is observed in conventional metals. This means that there is a phase difference of π between the Landau quantization in graphene and that in normal metals, and the phase difference is caused by the Berry's phase in graphene. This phase difference is shown as different origins in N of graphene and 5-nm-thick film of graphite in Fig.3b of Novoselov *et al.* [5].

One of the first observations of SdHOs in graphene is shown in the left figure of Fig.1.3. The SdHO on top (left figure, a) is measured at a fixed gate voltage and at $T = 10\text{K}$, and the oscillations on the bottom (left figure, b) are measured at different temperatures (20K, 80K, and 140K) and at a constant magnetic field $B = 12\text{T}$. The oscillations are more prominent at small V_g for $T = 80\text{K}$ and $T = 140\text{K}$, and damp as V_g increases. At a higher T , oscillation decays more drastically. According to Novoselov *et al.*, this dependence on T in the decay of SdHO is another unique characteristic observed in graphene. Their sample is fabricated from monolayer graphene mechanically exfoliated from graphite [5]. Observation of oscillations in magnetoresistance, namely SdHOs is a proof of 2D electronic systems since they show that the orbital dynamics of the systems are affected only by the magnetic field applied perpendicularly to the plane of the 2D system. However, the observation of QHE is a more definitive evidence for being a 2D system, and thus it is a classic technique used to show a two-dimensional nature [14]. Fig.1.4 shows the experimental study done by Tan *et al.* on the magnetotransport in their monolayer graphene Hall bar. R_{xy} clearly shows plateaus at $\nu = \pm 10, \pm 14, \pm 18$ where $\nu = 4(N + 1/2)$ for $N = \pm 0, \pm 1, \pm 2, \dots$, and they correspond to minima in R_{xx} , showing a strong SdHO. A highly symmetric feature implies the high homogeneity in their graphene sample. The mobility in their sample is $\sim 8,000 \text{ cm}^2\text{V}^{-1}\text{s}^{-1}$ and the Dirac point is at $V_D = 1.5\text{V}$. Graphene is mechanically exfoliated from graphite. Fig.2(a) in Zhang *et al.* shows quantization in both of R_{xx} and R_{xy} as a function of magnetic field B . Two well-defined plateaux are observed in R_{xx} for $B > 4\text{T}$, and SdHO is visible for lower B [32].

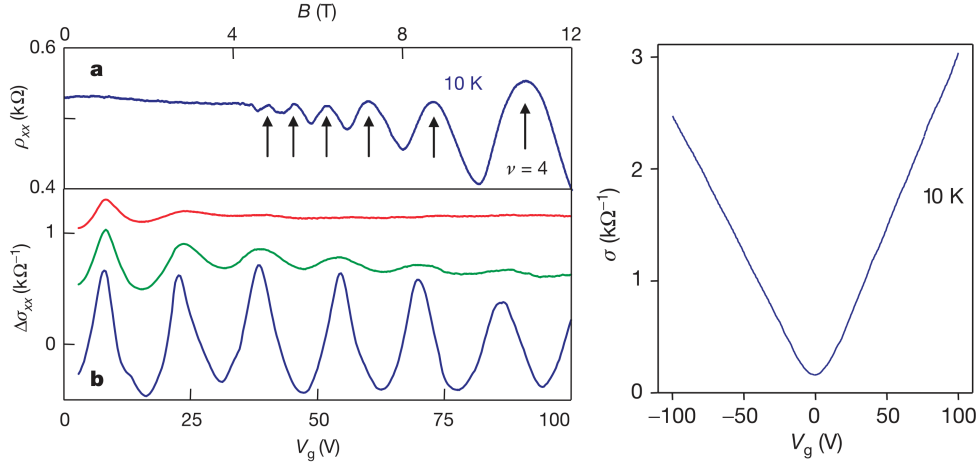


Figure 1.3: **Shubnikov-de Haas oscillations and conductivity minimum in graphene.** (Left, a) SdHO at constant gate voltage $V_g = -60$ V. (Left, b) SdHOs as a function of gate voltage at $T = 20$ K (blue), $T = 80$ K (green), and $T = 140$ K (red). (Right) Conductivity as a function of V_g measured at 10 K showing the electric field effect in graphene [5].

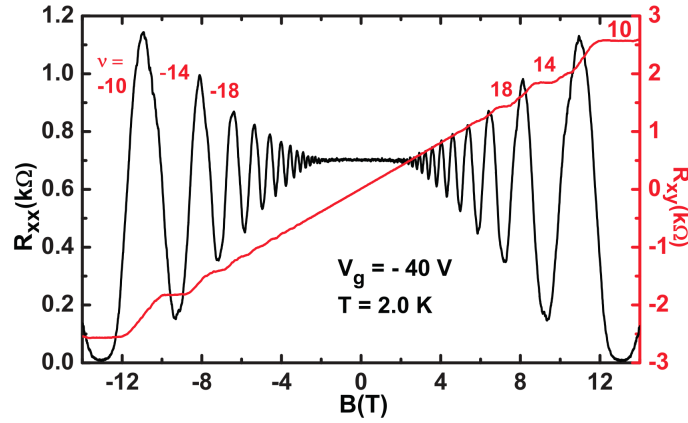


Figure 1.4: **Shubnikov-de Haas oscillations and QHE.** Magnetoresistance R_{xx} (black) and Hall resistance R_{xy} (red) measured at a fixed gate voltage $V_g = -40$ V and at temperature $T = 2.0$ K. [34]

The anomalous QHE, where Hall resistance is quantized at almost zero magnetic field, has been shown in some graphene devices including suspended bilayer graphene [35], and

Moiré heterostructures [36]. Moiré pattern is made from two graphene layers stacked together by the van der Waals forces and with some small twist angle in between the two lattice orientations. This lattice mismatch creates a periodicity with a longer wavelength than that of monolayer graphene in the lattice structure which for example, a twist angle of 1.08° leads to a wavelength of 13nm [37]. To fabricate high-quality graphene devices, hBN flakes are commonly used as a substrate to form hBN-graphene-hBN (hBN-Gr-hBN) heterostructures. Refer to chapter 2.1 for more discussion about graphene devices on hBN substrates. When forming a hBN-Gr-hBN heterostructure, there exists a relative angle between the bilayer graphene and the hBN, in addition to the interlayer twist angle between the two graphene layers. hBN layers are generally placed at a random angle on graphene, but it is possible to align the axes of hBN and graphene. Serlin *et al.* reported the anomalous QHE in Moiré graphene heterostructures where interlayer angle of twisted bilayer graphene is 1.1° with hBN aligned to the bilayer graphene. In this limit, the band structure of twisted bilayer graphene can be understood as an overlap of two Dirac dispersions with a shift in between, and this creates a gap in the band structure at the CNP with top and bottom flat bands with Chern numbers $C = +1$ and $C = -1$, respectively [36, 38]. They observe the zero-field Hall resistance being the strongest near a filling factor $\nu = 3$, which then implies the anomalous quantum Hall state possessing a Chern number $C = +1$, and the strong correlation breaks time reversal symmetry. Anomalous QHE has attracted significant effort in its possible applications such as topological quantum computing [39].

The efforts to achieve QHE with more relaxed experimental conditions such as higher temperatures are driven by the metrological field since the SI unit of resistance is defined based on the Hall resistance, which in theory is equal to $h/(ie^2)$ where i is an integer. QHE in conventional 2DEGs has been used in the metrology to define the resistance standard, and for 30 years, silicon MOSFETs (metal-oxide-semiconductor field-effect transistors) and III-V semiconductor devices had been used for its measurements [40]. The first characterization of the quantum Hall resistance standard in graphene was in 2008 by Giesbers *et al.* [41]. Their $1\mu\text{m}$ -wide graphene Hall bar samples showed equivalent quantum Hall resistance in conventional 2DEG field effect transistors, but the high-accuracy measurements in their experiments were limited mainly due to the high contact resistances and low breakdown currents of their samples. Their quantum Hall measurements were performed at $B = 14\text{T}$ and $T = 0.35\text{K}$. Tzalenchuk *et al.* demonstrated the accuracy of 3×10^{-9} with monolayer epitaxial graphene Hall bar on SiC substrate in 2010, when the precision achieved in graphene was still limited to below 1×10^{-6} [42]. There was a breakthrough in 2015 by Ribeiro-Palau *et al.*, where graphene Hall bars fabricated from CVD on SiC substrate achieved a significantly more relaxed experimental implementation of QHE with

1×10^{-9} accuracy for over a range of 10T. The commonly used devices for quantum Hall resistance standard are gallium arsenide (GaAs)/aluminum GaAs heterostructures, which for example, require $B = 10\text{T}$, $T = 1.3\text{K}$, and $I = 50\mu\text{A}$ [43]. Ribeiro-Palau *et al.* showed quantum Hall resistance standard with 5T, 5K and $50\mu\text{A}$ or 6T, 5K and $160\mu\text{A}$ [44].

Most of the graphene devices with high mobility ($>10,000 \text{ cm}^2\text{V}^{-1}\text{s}^{-1}$) so far have been fabricated with exfoliated graphene, and only a few studies have shown performances comparable to exfoliated ones using CVD graphene. Although graphene has shown promising electric and optical properties for future electronic devices, graphene still suffers from its low scalability. The ultimate goal of this research is to achieve high-performance devices with CVD graphene, and to find further applications of CVD graphene in nano-electronic devices. The research project was started by building the design of Hall bars and fabricating them with commercial CVD monolayer graphene. Characterization of quantum Hall effect was the first major goal to achieve with graphene Hall bars, and mobility in CVD graphene has to be relatively high ($>5,000 \text{ cm}^2\text{V}^{-1}\text{s}^{-1}$) for that to become possible. The quantized effects were not observed in the data presented in this study possibly due to the low quality of samples which may have originated from the fabrication process or the quality of the graphene. This research shows the fabrication methods of graphene Hall bars we developed and some of the transport properties of graphene characterized both at room and low temperatures. Some analysis comparing to the results in the literature is presented. Chapter 2 discusses about the fabrication of graphene Hall bars, and chapter 3 covers the results of transport properties of graphene. The contact resistance using two different kinds of metal is discussed at the end. Finally, chapter 4 talks about the annealing done on our samples to remove the impurities on the graphene surface and how the transport properties have changed after annealing.

Chapter 2

Fabrication

2.1 Geometry of graphene Hall bars

Fig.2.1(a) shows optical micrograph of a typical Hall bar fabricated with CVD grown monolayer graphene and Fig.2.1(b) is a schematic of a Hall bar. One chip has $1\text{ cm} \times 1\text{ cm}$ graphene and hBN on $1.5\text{ cm} \times 1.5\text{ cm}$ Si/SiO₂ substrate, and it consists of 80 Hall bars of which 40 devices have $W = 2\mu\text{m}$ and $L = 8\mu\text{m}$, and the remaining 40 devices have $W = 5\mu\text{m}$ and $L = 20\mu\text{m}$. The samples characterized for the data presented in the thesis have a 1~2 layer ($\sim 0.6\text{nm}$ thick) hBN as an insulating substrate. An addition of hBN substrates on graphene devices was first proposed by Dean *et al.* in 2010 [45]. SiO₂ substrates deteriorate the intrinsic electronic properties of graphene, and there was a need for a new kind of substrates that can retain the graphene quality. hBN is a wide-gap insulator and is also a 2D van der Waals material. hBN has a similar lattice structure to that of monolayer graphene, with their lattice mismatch of about 1.5%. hBN also possesses a low dielectric constant which makes it an ideal insulating layer for graphene devices [46]. Dean *et al.* demonstrated about an order of magnitude higher mobilities than those with graphene directly on Si/SiO₂ substrates by adding an hBN substrate. Since graphene is a 2D material, surface treatment during the fabrication process and the homogeneity of graphene directly affect the quality of the device. Therefore, graphene Hall bars tend to be small in a size ($W = 1\sim 2\mu\text{m}$ [30, 47]), and they are typically fabricated with electron-beam lithography (EBL). Fig.2.2 shows the design of Hall bars used in photolithography and the optical micrograph of a completed device. Single device has ten bonding pads of which eight are connected to graphene and two are not used. These two bonding pads originally served as contacts to back-gate. Our old fabrication process had a wet-etching of SiO₂

substrate with hydrofluoric acid (HF) solution all the way to the underlying Si substrate and a metal deposition into the etched part of SiO_2 so that the Si substrate (back-gate) is contacted. This process was then removed since HF can contaminate graphene and we developed a different method instead to contact back gate as described in sec.3.1.

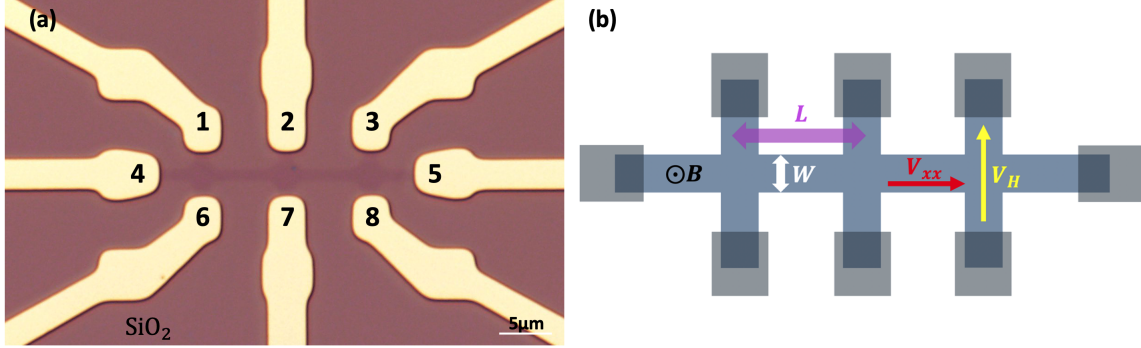


Figure 2.1: **(a) Optical micrograph of a Hall bar. (b) Schematic of a Hall bar.** (a) Graphene channel (dark purple color) is contacted by eight nickel (20nm)/gold (80nm) Ohmic contacts (gold color) and is on SiO_2/Si substrate. For the transport measurements, current flows from contact 4 (source) to contact 5 (drain) and magnetic field B is applied perpendicularly to the plane of the sample. The width and length of the Hall bar are $W = 2\mu\text{m}$ and $L = 8\mu\text{m}$, respectively. Hall voltage (V_H) is measured across contact 1-6, 2-7, or 3-8, and the longitudinal voltage (V_{xx}) is measured across contact 1-2, 2-3, 1-3, 6-7, 7-8, or 6-8.

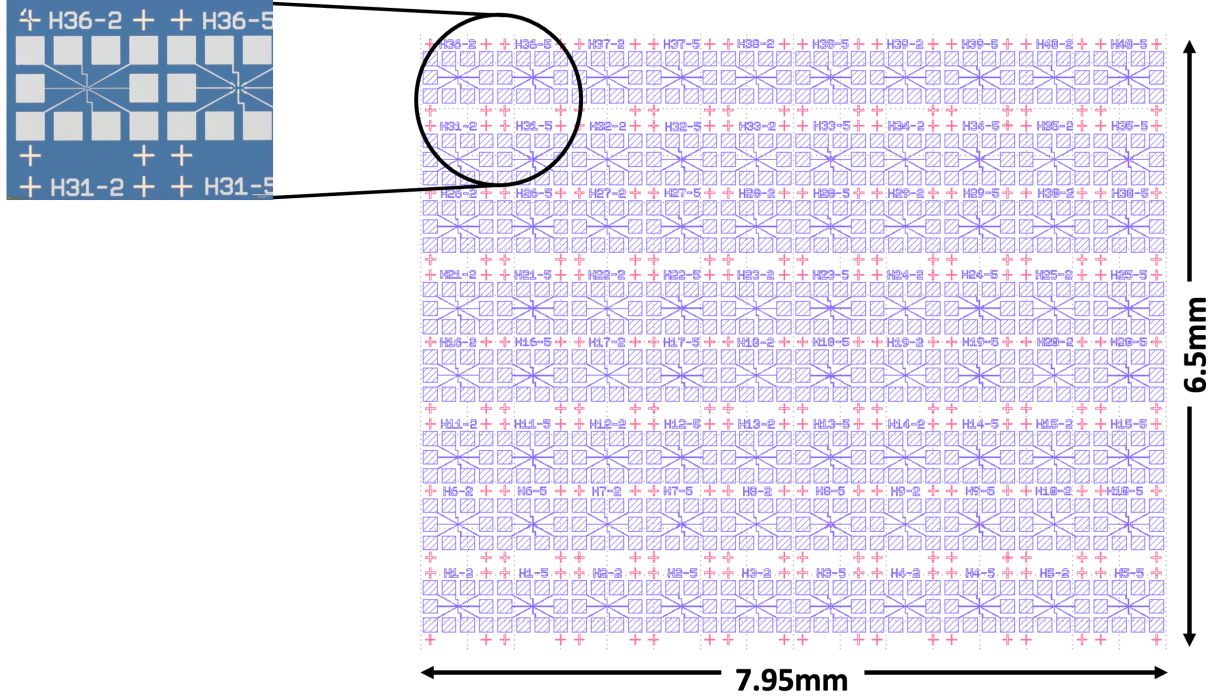


Figure 2.2: **Chip design.** Photolithography design of Hall bars showing 80 devices. Optical micrograph of a single device is also shown. A graphene Hall bar is connected to eight bonding pads. The image shows ten bonding pads of which two are not used.

2.2 Fabrication process of Hall bars

Graphene devices are made from 1cm²-sized monolayer graphene and 1~2 layer hBN on Si/SiO₂ substrates (Grolltex monolayer graphene on 0.6nm hBN on 285nm SiO₂). The sheet resistance, the Raman D/G ratio, and the mobility of FET on SiO₂ of graphene provided by the supplier is 430±50Ω/sq, 0.02, and >2,700cm²/Vs, respectively. Graphene Hall bars are fabricated with photolithographic patterning and O₂ plasma etching. The fabrication processes are classified into three main steps as listed below:

1. Pattern alignment marks
 - (a) Pre-process baking
 - (b) Photolithography to pattern alignment marks¹

¹Marks to align subsequent photolithography masks

- (c) Etch graphene inside alignment marks²
- (d) Metallization
- (e) Liftoff

2. Pattern graphene channels

- (a) Pre-process baking
- (b) Photolithography to pattern graphene channel
- (c) Etch graphene outside of the channels
- (d) Remove resists

3. Pattern electrodes

- (a) Pre-process baking
- (b) Photolithography to pattern electrodes
- (c) Metallization
- (d) Liftoff
- (e) Post-process baking

More detailed fabrication steps are described in section [A.1](#) Fig. [2.3](#) is a scanning electron micrograph (SEM) showing a section of one of our graphene Hall bars with size $W = 20\mu\text{m}$. Graphene is highly sensitive to typical fabrication processes such as spin coating of resist in lithography or liftoff in metalization. We found that the most crucial fabrication process that led to significant damages on graphene was the first resist coating done on the sample. Water molecules get trapped underneath graphene when graphene is exposed to ambient conditions, and this leads to a less adhesion of graphene on underlying substrates. We addressed the issue by baking the sample at 180°C in an oven with N_2 gas, and removing the water molecules on the sample. We also noticed that the resist spin-coating with a fast acceleration may tear graphene, and thus used a low acceleration (see section. [A.1](#) for a detailed spin-coating recipe). Because we used large scale CVD graphene to fabricate many Hall bars on one chip, the yield relies on the fabrication which causes less damage in graphene. In Fig. [2.3](#), some inhomogeneity inside the graphene channel is observed from the contrast in its color which could possibly be the surface roughness of underlying SiO_2 that is made more noticeable by the presence of graphene. A few holes, wrinkles, and particles are also observed on graphene.

²Graphene has to be removed for metal to be directly deposited on SiO_2

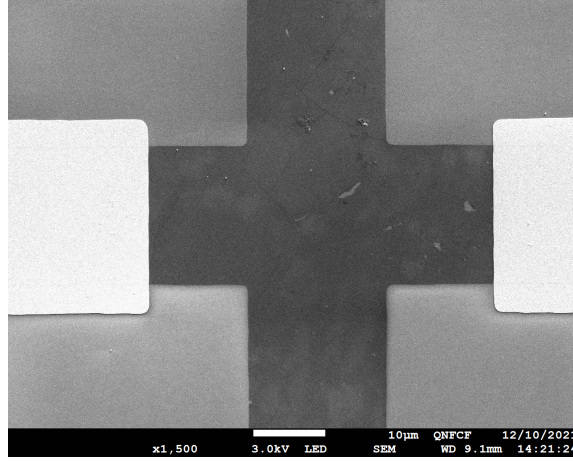


Figure 2.3: **SEM image of a Hall bar.** A section of graphene Hall bar with $W = 20\mu\text{m}$ contacted by titanium (20nm)/gold (80nm). Gray area is the SiO_2 and the darker gray area is the graphene channel which is directly on the SiO_2/Si substrate with no underlying hBN. White area is the electrodes. The samples characterized for the data presented in this thesis have either nickel (20nm)/gold (80nm) or palladium (50nm) electrodes. Scale bar shows $10\mu\text{m}$. Image was taken with JEOL JSM-7200F at the QNFCF.

Chapter 3

Characterization

3.1 Contacting back-gate

Si substrate with a resistivity of $<0.005\Omega\cdot\text{cm}$ is used as a back-gate in our samples. To contact the back-gate, we patterned gold layer on SiO_2 outside the device area of samples, and made a few lines of scratch through it with a diamond scribe to paste silver epoxy on top of the scratches. Silver epoxy is left in ambient conditions for ~ 8 hours before pasting it on the sample since otherwise its viscosity is too low and it can reach and contaminate the devices. The same gold layer is then wire-bonded. The carrier density of graphene can be varied by applying external voltage to the back gate through electric field effect.

3.2 Transport properties of graphene

Two different chips are measured to characterize the transport properties of graphene. Each chip contains 80 Hall bars in total, of which the geometry and dimension are described in chapter 2.1. In the following sections, these chips will be referred to as A and B. Fabricated chips are observed by the optical microscope to check each Hall bar and the Hall bars without any visible defects and impurities on the device and especially on graphene surface are picked for characterization purposes. After that, electrical continuity is tested on each of the chosen Hall bars using two probes at the probe station. Transport is characterized on four different Hall bars on each of chip A and chip B, and these Hall bars are referred to as 1 through 4 throughout the thesis. For example, a specific Hall bar is referred to as sample A1. The difference in the fabrication process of chip A and B is the metal deposited

Sample	W/L	Electrode
A1	5 μ m/20 μ m	Ni/Au
A2	2 μ m/8 μ m	Ni/Au
A3	5 μ m/20 μ m	Ni/Au
A4	5 μ m/20 μ m	Ni/Au
B1	2 μ m/8 μ m	Pd
B2	2 μ m/8 μ m	Pd
B3	2 μ m/8 μ m	Pd
B4	2 μ m/8 μ m	Pd

Table 3.1: **Dimension and metals used for electrodes in the characterized samples.** First column: sample number. Second column: width and length of the Hall bar. Third column: metals used to contact graphene.

to contact graphene. A has nickel (Ni)/gold (Au) Ohmic contacts and B has palladium (Pd) Ohmic contacts. Some of the details of each sample are listed in Table.3.1. Fabricated chip is mounted on a chip holder, and then one sample (one Hall bar) is bonded using the Westbond 7476E Manual Wirebonder with aluminum wires for characterization. Samples are cooled down to ~ 1.6 K using the Janis 1.5K cryostat for low temperature measurements. The data presented in the thesis is taken using a standard two-terminal or four-terminal lock-in technique (Stanford Research Systems Model SR830DSP Lock-in amplifier).

3.2.1 Magneto-transport in graphene

Fig.3.1 shows the magnetoresistance and the Hall resistance as a function of gate voltage at a fixed magnetic field obtained by four-terminal measurements with constant current. A four-terminal method passes a small constant current between the outer two probes, and the voltage is measured across the inner two probes [8]. Resistance values are found by measuring the four-terminal voltage V and using the relation $R = V/I$ where I is the AC excitation current converted from the low-frequency AC voltage generated by a lock-in amplifier. The Dirac points are confirmed by the sign change in R_{xy} which occurs due to the change in the charge carriers from holes to electrons. There are slight shifts from Dirac point (V_D) in each R_{xx} to V_{bg} where sign changes. Fig.3.2 shows the magnetoresistance and the Hall resistance as a function of magnetic field from -0.2 T to 5 T at a fixed gate voltage, measured on the sample A3. The Hall resistance shows a linear dependence in

B that passes the origin as expected in a disordered graphene. No quantized resistance is observed. The mobility and the density of this sample at the measured gate voltage ($V_{bg} = 20V$) are $3,243 \text{ cm}^2V^{-1}s^{-1}$ and $9.77 \times 10^{11}/\text{cm}^2$, respectively, and these values are obtained after current annealing (see [chapter 4](#) for more details on current annealing). [Fig.3.3](#) shows the magnetoresistance as a function of magnetic field from $-0.2T$ to $5T$ at a fixed gate voltage, measured on the sample A1. R_{xx} in both [Fig.3.2](#) and [Fig.3.3](#) exhibit a parabolic dependence in B . This is a behavior observed in a few-layer graphene as demonstrated by Gopinadhan *et al.* where R_{xx} measured on their four-layer graphene on BN at $T = 400K$ is proportional to $1 + (\mu B)^2$ where μ is mobility and B is magnetic field. Note that their measurement is not taken at low temperature $\sim 1.5K$. We expect the temperature dependence of magnetoresistance in graphene outside of the quantum regime to be not significant [\[48\]](#). The mobility and the density of this sample at the measured gate voltage ($V_{bg} = 10V$) is $2,769 \text{ cm}^2V^{-1}s^{-1}$ and $9.69 \times 10^{11}/\text{cm}^2$, respectively, and these values are obtained after annealing. [Fig.3.4](#) shows the magnetoresistance as a function of magnetic field $0.1T$ to $-5T$ at a fixed gate voltage, measured on the sample A2. The data contains large noise, but R_{xx} exhibits an overall linear dependence on B unlike the parabolic dependence seen in [Fig.3.2](#) and [Fig.3.3](#). The mobility and the density of this sample at the measured gate voltage ($V_{bg} = 20V$) is $2,461 \text{ cm}^2V^{-1}s^{-1}$ and $8.94 \times 10^{11}/\text{cm}^2$, respectively, and these values are obtained before annealing. No Shubnikov–de Haas effect is observed in the magnetoresistance for any of the samples studied here. [Fig.3.3](#) and [Fig.3.4](#) show the expected symmetry around $B = 0$ and this result also agrees with the magnetoresistance presented in Gopinadhan *et al.* [\[48\]](#).

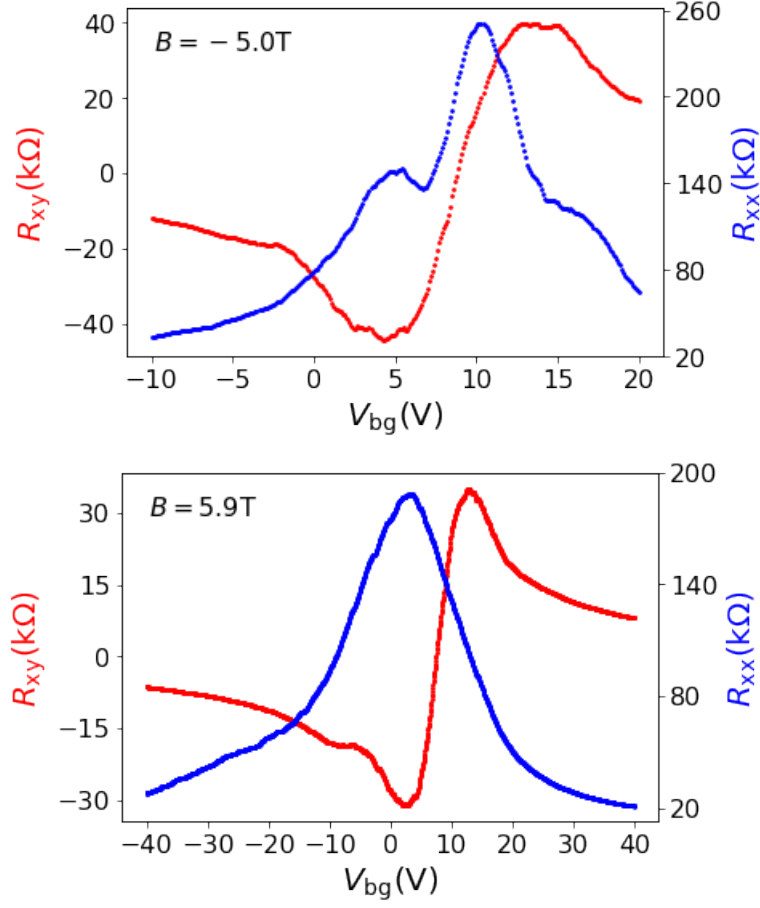


Figure 3.1: **Magnetotransport as a function of back gate voltage.** Magnetoresistance (right axis) and Hall resistance (left axis) as a function of gate voltage measured at $B = -5\text{T}$ and $T = 1.66\text{K}$ from sample A2 (top) and $B = 5.9\text{T}$ and $T = 1.65\text{K}$ from sample A3 (bottom). Both measurements were performed with four-terminal constant AC excitation current at $I = 100\text{nA}$.

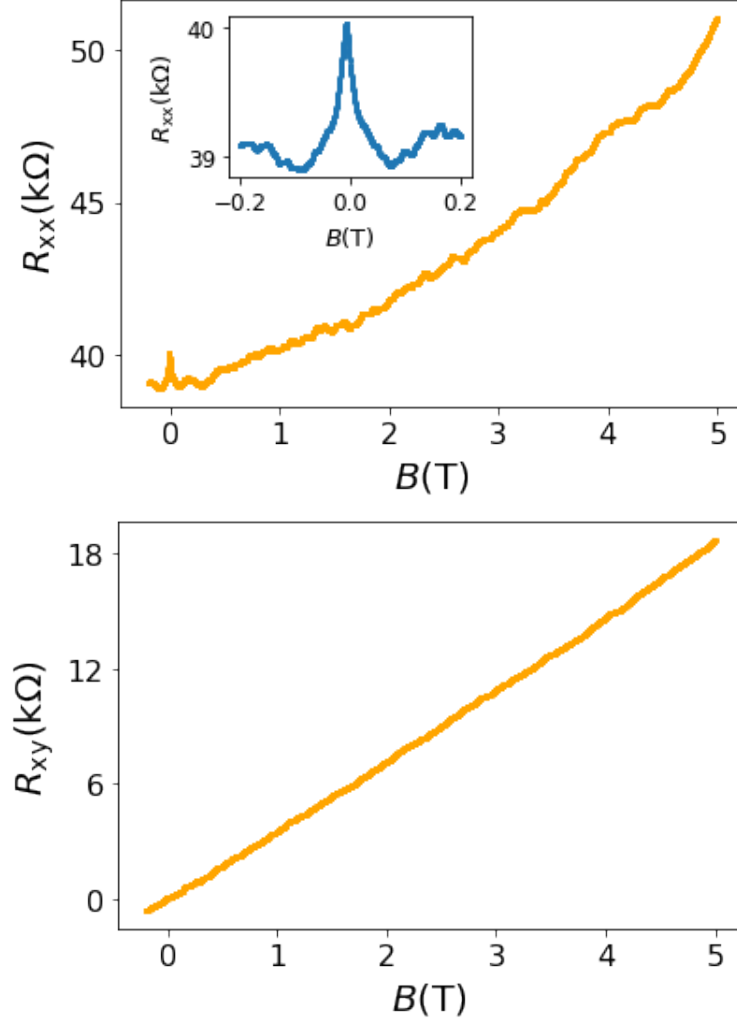


Figure 3.2: **Magnetotransport as a function of magnetic field.** (Top) Magnetoresistance R_{xx} from 0T to 5T at a fixed gate voltage $V_{bg} = 20\text{V}$ and $T = 1.64\text{K}$. Inset shows the weak-localization signal near $B = 0\text{T}$ from the same data. Measurement was taken from sample A3. (Bottom) Hall resistance at $V_{bg} = 20\text{V}$ and $T = 1.64\text{K}$ measured on a sample A3. Both measurements were performed with four-terminal AC current at $I = 100\text{nA}$.

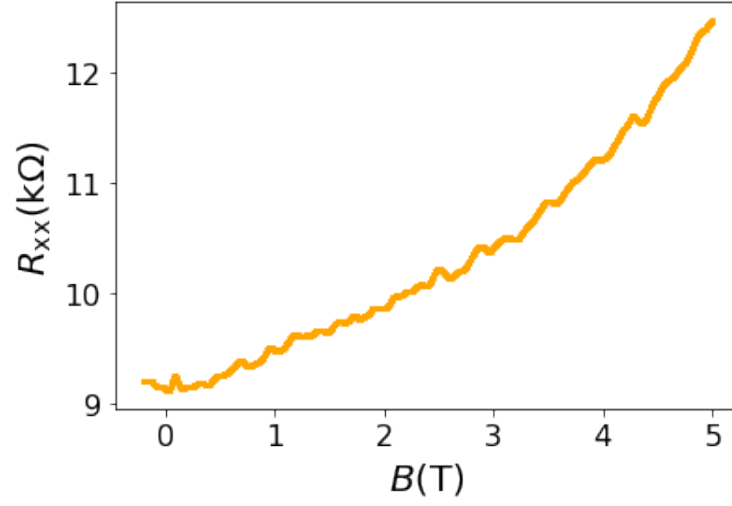


Figure 3.3: **Magnetotransport as a function of magnetic field.** Magnetoresistance R_{xx} from 0T to 5T at a fixed gate voltage $V_{bg} = 10V$ and $T = 1.64K$. Measurement is taken from sample A1 with four-terminal AC current at $I = 100nA$.

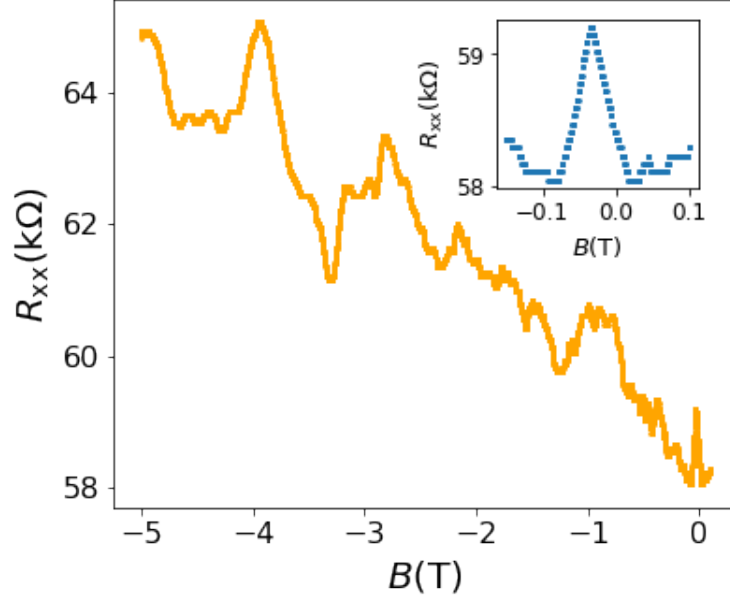


Figure 3.4: **Magnetotransport as a function of magnetic field.** Magnetoresistance R_{xx} from 0T to -5 T at a fixed gate voltage $V_{bg} = 20$ V and $T = 1.65$ K. Measurement is taken from sample A2 with four-terminal AC current at $I = 100$ nA. Inset shows the weak-localization near $B = 0$ T from the same data. Data contains artifacts due to the resolution of the lock-in amplifier being set low in this particular measurement.

3.2.2 Electronic mobility and density

Through electric field effect, the density of charge carriers in graphene can be tuned by applying gate voltages, and graphene can either be p -doped or n -doped [5]. Fig.3.5 and Fig.3.6 show the gate voltage dependence of the graphene carrier density n_{gr} . Green lines in all figures show linear regression with a function $n_{gr} = \alpha V_{bg} + n_0$ where n_0 is the value of n_{gr} at which the lines intercept the vertical axis. Data in Fig.3.5 is obtained from sample A1. The values of $|\alpha|$ extracted before current annealing is $5.56 \times 10^{10} \text{ cm}^{-2}\text{V}^{-1}$ and $6.52 \times 10^{10} \text{ cm}^{-2}\text{V}^{-1}$. The values of $|\alpha|$ extracted after current annealing is $5.19 \times 10^{10} \text{ cm}^{-2}\text{V}^{-1}$ and $5.18 \times 10^{10} \text{ cm}^{-2}\text{V}^{-1}$. The value of α in Novoselov *et al.* is $\alpha \approx 7.3 \times 10^{10} \text{ cm}^{-2}\text{V}^{-1}$ [5]. Fig.3.6 is obtained from sample A3. The values of $|\alpha|$ extracted before current annealing is $6.41 \times 10^{10} \text{ cm}^{-2}\text{V}^{-1}$ and $6.21 \times 10^{10} \text{ cm}^{-2}\text{V}^{-1}$. The values of $|\alpha|$ extracted after current annealing is $6.10 \times 10^{10} \text{ cm}^{-2}\text{V}^{-1}$ and $5.42 \times 10^{10} \text{ cm}^{-2}\text{V}^{-1}$. These figures show that as V_{bg} is swept from -40 V to 40 V, the density linearly decreases towards the Dirac point,

and linearly increases afterwards. The electronic density is determined with the relation $n = IB/eV_H$ where I is the source-drain current, B is the applied magnetic field, V_H is the Hall voltage, and e is the elementary charge. Since the magnetic field applied to measure the density is small ($B = \pm 0.2\text{T}$), offset in V_H can be non-negligible, and thus V_H was found by measuring V_{xy} at $B = \pm 0.2\text{T}$, and used the relation $V_H = (V_{xy,+B} - V_{xy,-B})/2$. Density values were measured around the V_D , but are omitted in the presented data since fluctuations in the measured V_{xy} were large and the corresponding n_{gr} values were not reliable. However, it is also known that density as a function of gate voltage behaves uniquely around the Dirac point. The density can never be tuned to zero by changing the gate voltage. Fig.6 in the review of Peres [3] shows the measurement of density vs gate voltage that follows the relation $n_{gr} = \alpha V_{bg}$, but the linear dependence no longer exists around the Dirac point, and density seems to have a finite minimum value. The system shows charge-density fluctuations around the Dirac point that are caused by the electrostatic potential originating from the charged impurities. The system surface has a spatially varying potential caused by the charge puddles [3].

Fig.3.7 shows the mobility measured at different gate voltage. All samples except for A3 have the general trend such that the mobility becomes particularly lower around the Dirac point V_D . This is an expected behavior since density goes to zero as V_{bg} becomes closer to CNP and in theory, mobility does not exist at zero density. Our mobility as a function of density did not show an expected behavior where mobility has a peak and reaches its maximum around zero density. As a reference, Fig.5(d) in De Fazio *et al.* shows a mobility vs density curve [11]. Fig.1(a) in Zhang *et al.* shows change in mobility and density as a function of gate voltage. Mobility reaches the highest value around $V_g = 0\text{V}$ and corresponding density is close to zero [32]. We expect the highest mobility near V_D , and we observe in some samples shown in Fig.3.7 relatively higher mobilities around V_D . Sample A3 also shows a dip around the same range of V_{bg} , and significantly higher mobilities close to V_D , but the mobilities are lower as V_{bg} is varied away from V_D . Sample B's have lower average mobility than sample A's, and mobilities in Sample A's show a higher variation than sample B's. One possible cause that lowered mobilities in sample B's is the residue of photoresist that was hardened by the O_2 plasma etching and could not be removed. A clearly larger amount of photoresist residue was observed with optical microscope on sample B's compared to sample A's, and higher V_D values in sample B's confirm the larger amount of impurities. An optical image of the photoresist residue is shown in Fig.A.1. Mobility was found by using the relation $\mu = I(L/W)/enV_{xx}$ where L/W is the length to width ratio of the Hall bar, n is the density, and V_{xx} is the longitudinal voltage measured across the whole Hall bar or through the half of the Hall bar. The highest mobility and lowest density among all samples was $3,327 \text{ cm}^2\text{V}^{-1}\text{s}^{-1}$ at $V_{bg} = 20\text{V}$ obtained

from sample A1 after annealing and $7.16 \times 10^{11} \text{ cm}^{-2}$ at $V_{\text{bg}} = 0\text{V}$ from sample A2 before annealing, respectively. Samples A1 and A3 show similar values in density, but there is a large difference in their corresponding mobility values between the two samples.

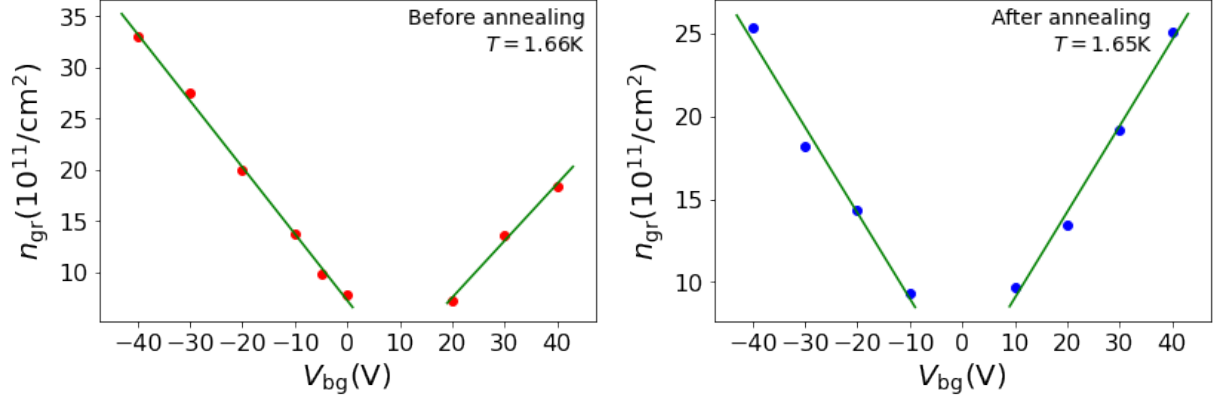


Figure 3.5: **Density dependence on back gate voltage.** The absolute value of carrier density of graphene vs back gate voltage (V_{bg}) before (left) and after (right) annealing measured with four-terminal AC current at $I = 100\text{nA}$ and $B = \pm 0.2\text{T}$. Measurement was taken from sample A1. Dirac point is at $V_{\text{D}} = 11.8\text{V}$ before annealing at RT and $V_{\text{D}} = -16.4\text{V}$ and $V_{\text{D}} = -7\text{V}$ after annealing at RT.

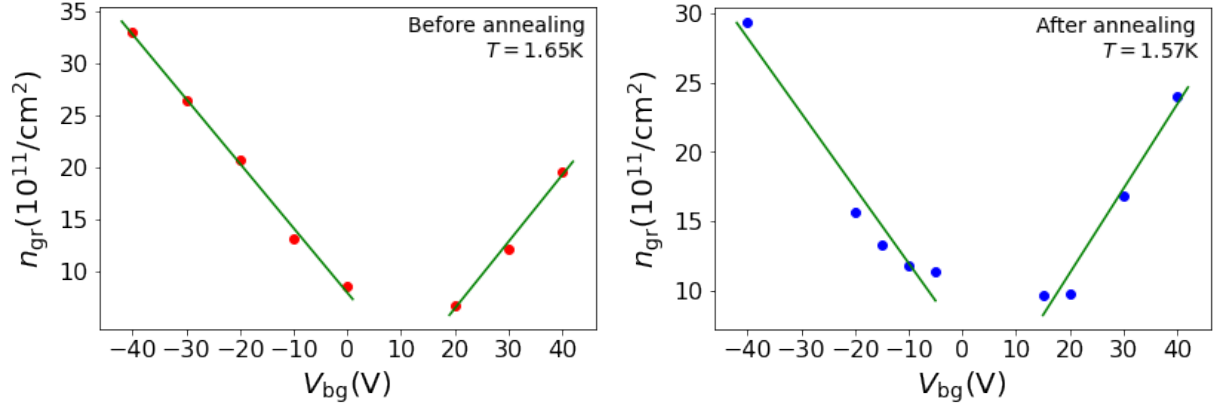


Figure 3.6: **Density dependence on back gate voltage.** The absolute value of carrier density of graphene vs back gate voltage (V_{bg}) before (left) and after (right) annealing. Measurements are taken at $B = \pm 0.2\text{T}$ with four-terminal AC current $I = 100\text{nA}$ (before annealing) and $I = 500\text{nA}$ (after annealing) from sample A3. Dirac point is measured at $V_D = 9.68\text{V}$ before annealing at RT. A broad peak in graphene resistance vs V_{bg} is obtained after annealing at RT with Dirac point around $V_{bg} = 0\text{V}$.

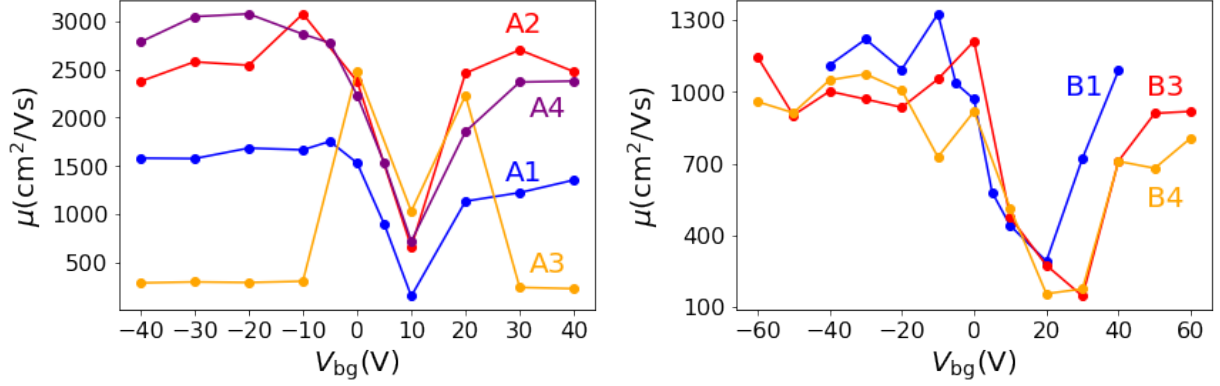


Figure 3.7: **Mobility vs back gate voltage.** (Left) Mobility measured on samples A1–A4 at different V_{bg} before annealing. The Dirac points measured on samples A1–A4 are $V_D = 13\text{V}$, $V_D = 7\text{V}$, $V_D = 11\text{V}$, $V_D = 16.4\text{V}$, respectively. Corresponding mobility values show dips around $V_{bg} = 10\text{V}$. (Right) Mobility measured on samples B1, B3, and B4 at different V_{bg} before annealing. The Dirac points measured on these samples are $V_D = 23.2\text{V}$, $V_D = 28.5\text{V}$, and $V_D = 25\text{V}$, respectively. Corresponding mobility values have dips around $V_{bg} = 25\text{V}$. All of the mobility measurements in both figures are taken around $T = 1.6\text{K}$ and at $B = \pm 0.2\text{T}$.

3.2.3 Dependence of resistance on gate voltage

Fig.3.8 shows a typical gate voltage dependence of the graphene resistance measured at room temperature (RT) and at $T = 1.64\text{K}$. Applying $V_{bg} > V_D$ tunes E_F into valence band and dopes graphene where carriers are electrons, and applying $V_{bg} < V_D$ tunes E_F into conduction band and dopes graphene where holes are the carriers. As V_{bg} is varied from -40V to more positive values, E_F approaches the Dirac point at which the density of states vanishes, and carrier density is reduced. The resistance reaches maximum at the Dirac point, and thus we know that graphene is charge-neutral at the corresponding V_{bg} . The resistance curves show broad peaks at $41\text{k}\Omega$ at RT and $43\text{k}\Omega$ at $T = 1.64\text{K}$ which are typical resistance values measured from our samples. Generally, resistance measured at low temperature is slightly lower than that measured at RT for $|V_{bg}| \gg V_D$ and has higher resistance than that measured at RT at the peak, meaning that graphene is slightly more resistive at low temperature than at RT at the Dirac point. Additionally, V_D is at a slightly higher V_{bg} at low temperature than at RT. Overall, we did not observe a significant temperature dependence in the resistance of graphene and in the value of V_D . Tempera-

ture dependence becomes apparent in the electronic transport when the electron-phonon interactions are the most dominant source of scattering mechanisms. Other scattering mechanisms such as topographic corrugations and ionized and charged impurities are more dominant in our samples. Graphene without any source of charged impurities is electrically neutral and such graphene has its CNP at zero gate voltage. However, fabricated graphene devices are generally doped by impurities which shift the CNP to positive gate voltages. In fact, most of the data on the resistance of graphene from our samples show a Dirac point at positive gate voltages, and thus graphene is *p*-doped at zero gate voltage. We also noticed that the width of graphene resistance curves in our samples are much larger than those reported in the literature with higher graphene mobility than that measured in our samples. In theory, undoped graphene has a Dirac point at zero gate voltage, and thus these results show the extent of disorder in our samples.

It is also common to show the electric field effect in graphene through conductivity as a function of gate voltage, as shown in the right figure of Fig.1.3. The conductivity has a minimum at V_D as graphene is described by the Dirac equation. The value of minimum conductivity is known to be one conductivity quantum, e^2/h . Since the mean free path λ of carriers cannot be smaller than their wavelength, the conductivity σ can be written as $\sigma = (e^2/h)k_F\lambda$ which implies that σ cannot be smaller than e^2/h . However, this explanation is true only in a metal without localization which is caused by the disorder in the system, and it fails in the 2D electronic systems with disorder. In theory, localization effects are not expected in 2D Dirac Fermions, and therefore, this argument should be true in graphene. Mobility $\mu = \sigma/ne = 15,000 \text{ cm}^2 \text{ V}^{-1} \text{ s}^{-1}$ in their graphene device was found from the linear dependence of σ on V_g . [5]. Our resistance curve is more parabolic than linear, and this observation indicates a higher disorder than graphene devices showing linear dependence in $\sigma(V_{bg})$.

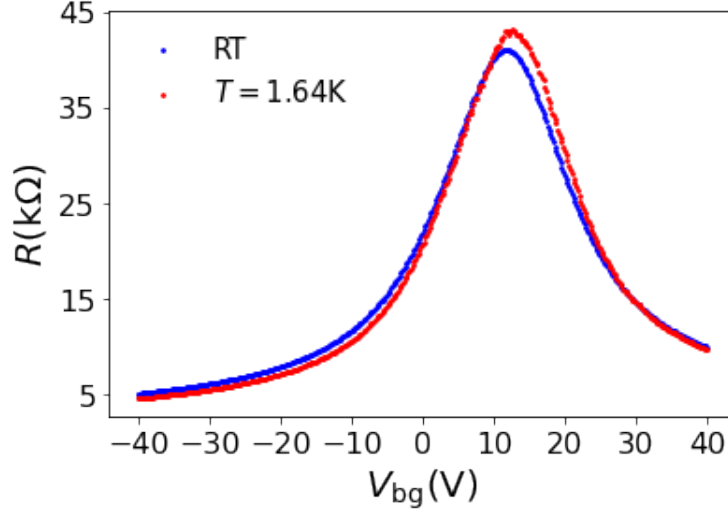


Figure 3.8: **Four-terminal resistance at room temperature (blue) and low temperature (red) measured at zero magnetic field.** Dirac points are $V_D = 12.2\text{V}$ and $V_D = 13.2\text{V}$ at RT and at $T = 1.64\text{K}$, respectively. The measurements at RT and $T = 1.64\text{K}$ were taken with a four-terminal AC excitation current at $I = 100\text{nA}$ from sample A1 before annealing.

3.2.4 Disorder and weak localization in graphene

Weak localization (WL) and weak anti-localization (WAL) are a quantum localization effect observed in low-dimensional disordered conductors through scattering of electrons. They are the quantum interference effects observed in magnetoresistance in the low-field limit as a precursor of the Anderson localization, which is also known as the strong localization. Conductivity is suppressed or enhanced at very low temperatures in WL or WAL, respectively. WL and WAL are one of the phenomena characterized to demonstrate the proximity spin-orbit coupling in various Van der Waals heterostructures such as graphene on WS_2 [49, 50]. Disorder in solids are generally caused by impurities or defects. Charge carriers in an ideal graphene behave as Dirac fermions, and the symmetry in the pseudospin of graphene makes the electronic states insensitive to sources of elastic disorder [1]. These innate natures of graphene result in high mobilities as reported in the literature [9]. However in reality, the charge carriers are subject to many types of perturbations. In graphene, corrugation [51] and charge puddles [52] are the two most significant types of disorder that limit carrier mobility and lead to the suppression of expected WAL [53].

Charge puddles are inhomogeneities in electron density caused by locally varied electrostatic potential. There are many possible sources of disorder in graphene such as the roughness in the oxide substrate, structural defects in graphene, and ionized and charged impurities etc. The types of scattering sources also depend on the mobility of the device [54]. These origins of disorder in graphene are thus important factors to study for the advancement in graphene nano-electronic devices. In disordered systems, impurities deflect the free propagation of electrons. The mean free path λ in these environments is much smaller than the sample size. This regime is referred to as the diffusive transport. In contrast, the ballistic transport is the electronic transport when the mean free path is greater than sample size. Another characteristic that describes the electronic transport in solids is the phase coherence length λ_ϕ , which is the average distance an electron can travel while maintaining its phase coherence. In the diffusive regime, the electronic transport is in the quantum diffusive regime for the limit $\lambda_\phi \gg \lambda$. This limit means that the electrons can maintain the phase coherence for a long distance after being scattered. This results in the phase interference of electron trajectories, which are identical upon time-reversal symmetry. This causes the corrections to the semiclassical conductivity. This usual classical terms of the conductivity is the Drude conductivity, and the weak localization is the quantum correction term [1, 55].

We observed the WL in our magnetoresistance data. Fig.3.9 shows the weak localization at different back gate voltage. For clarity, the minimum value of resistance in each curve is subtracted, and the difference ΔR is shown. The WL is centered around $B = 0\text{T}$ since applying magnetic field B breaks down time-reversal symmetry, and thus WL is suppressed as B increases. The peaks have a characteristic of having a pointier peak on top of a broader peak, which has also been seen in other literature studies on WL [56] or the Anderson localization [57]. Our results clearly show suppressed or enhanced WL as V_{bg} changes. The dependence of WL in monolayer graphene on the gate voltage has not been studied widely as far as our knowledge is concerned. Some of our magnetoresistance data show more prominent WL than others as shown in the insets of Fig.3.2–3.4. Morozov *et al.* shows that the WL in the magnetoresistance of monolayer graphene is suppressed whereas multi-layer graphene exhibits standard WL. They saw WL in only a few of their monolayer graphene devices, and many devices did not show any sign of WL or WAL [6]. Similar results are demonstrated by Liu *et al.* where WAL instead of WL is observed in monolayer graphene whereas WL is observed in bilayer graphene magnetoresistance, and the magnitude of WL is enhanced as the number of graphene layers increases [56]. The characterizations of WL and WAL help understand the extent of disorder in graphene devices.

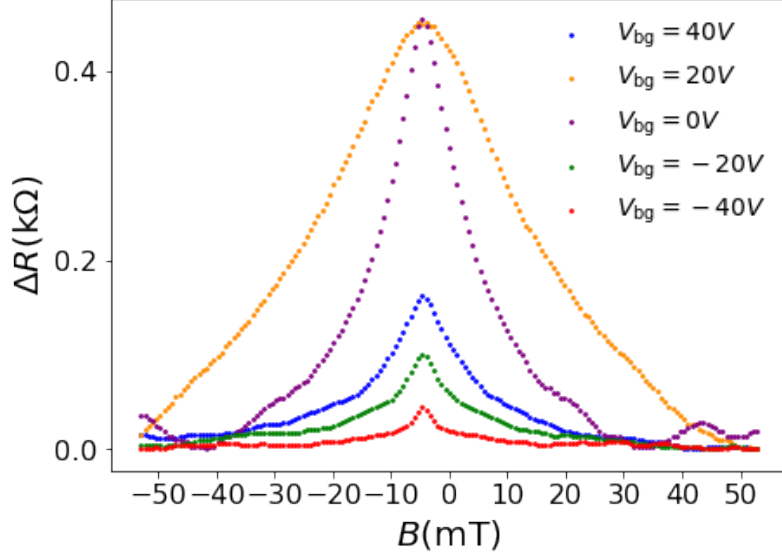


Figure 3.9: **Weak localization in graphene at different gate voltages.** Measurements are taken before annealing from sample A4 at $T = 1.64\text{K}$ with four-terminal constant AC current at $I = 100\text{nA}$ for the $V_{\text{bg}} = 0\text{V}$ measurement, and at $I = 500\text{nA}$ for the rest of the gate voltages. Dirac point in this sample was measured at $V_{\text{D}} = 12.8\text{V}$ at RT.

3.3 Ni/Au and Pd Ohmic contacts

Different materials used for Ohmic electrodes can lead to different contact resistance (R_{C}) at the graphene-metal interface, and the quality of contacts may have a large impact on the overall performance of graphene devices. The most commonly used metals for contacting graphene is chromium (Cr)/gold (Au) [10, 35, 58, 59] where Cr serves as an adhesion layer. Au is commonly used as Ohmic contacts since it does not oxidize, and is easier than other metals to bond to. However, improvements in contact resistance may not be the most crucial aspect in many experiments involving graphene devices. Some variable factors rather than the used materials themselves can affect the contact resistance, and it may simply be not straightforward to determine them. It may also depend on the conditions such as deposition temperature and rate during the metallization process of device fabrication, and photoresist residues generally increase the contact resistance. Due to these possible reasons, there is a variety of experimentally measured values of (R_{C}) in the literature for the same material. Cusati *et al.* discusses sheet resistance of graphene and the

formation of covalent bonds at the graphene-metal interface as important factors in contact resistances, and experimentally show that the contact resistance is linearly dependent on the sheet resistance of graphene in all of five different metals [60].

Choosing the right metals for contacting graphene becomes more relevant in metrology because it is desired to achieve as smaller contact resistance as possible in graphene devices to improve the precision in the resistance standard [44]. Ribeiro-Palau *et al.* achieved low contact resistances $\leq 1.2\Omega$ between graphene and titanium/palladium (60nm)/Au (20nm) Ohmic contacts where titanium (Ti) is an ultra-thin layer deposited for adhesion in their work on quantum Hall resistance standard in CVD graphene discussed in section 1.2.2 [44]. Tzalenchuk *et al.* reported $\approx 1.5\Omega$ contact resistances in their epitaxial graphene Hall bars contacted by Ti/Au (3/100nm) [42]. Janssen *et al.* also showed a few Ohms for the contact resistance of their epitaxial graphene Hall bars with Ti/Au (3/100nm) Ohmic contacts in their work to compare the quantum Hall resistances in graphene and GaAs/AlGaAs heterostructure [61]. There are some previous studies showing relatively low contact resistances obtained with Pd or Ni, and higher contact resistances with Ti, Cr, and aluminum (Al) [62–64].

Song *et al.* characterized the work function values of graphene under different metals through capacitance-voltage measurements using metal-graphene-oxide-semiconductor capacitor structure. The work function is the energy difference between the vacuum level and the Fermi energy [8], and can be one of the factors affecting the contact resistance. Their results show that there is no particular correlation between higher work functions of graphene under the metal and lower resistances, and Pd provides the lowest contact resistance amongst Au, Pd, Ni, and Cr/Au electrodes [65]. Our study compares the metal-graphene R_C with Pd contacts and Ni/Au contacts.

R_C of metal is determined as follows. The resistance of graphene R_{gr} in each pair of contacts is determined by measuring V_{xx} with a four-terminal measurement at a constant excitation current of $I = 100\text{nA}$ and calculating the sheet resistance of graphene. The total resistance R_{tot} in each pair is found by $R_{tot} = V_{exc}/I$ with a two-terminal measurement with a constant excitation voltage at $V_{exc} = 100\mu\text{V}$ where I is the measured current. R_{gr} is then subtracted from R_{tot} . The remaining resistance is the resistance originated from the two metal-graphene interfaces ($2 \times R_C$). Finally, contact resistivity ($\Omega \cdot \mu\text{m}^2$) of metal is determined since R_C is measured with different areas of graphene-metal interfaces. Measurements were taken from three different pairs of contacts from all of the samples except for A2, namely, samples A1, A3, A4, B1, B2, B3, and B4. The histograms in Fig. 3.10 compare the contact resistivity of Pd and Ni/Au contacts. Ni/Au contacts show a much broader range of resistivity than Pd contacts. Nonetheless, Pd contacts provided much lower contact resistance than Ni/Au. These results are consistent with other studies

described above where Pd generally provides lower contact resistances. However, only one chip was characterized for each metal. This means that all of the measurements for each metal are taken from samples that are fabricated at the same time. Thus, the data does not take into account the variation in resistances that fabrication may have caused. Also, note that samples A1, A3, and A4 have $W = 5\mu\text{m}$ which gives an interface area of $31.25\mu\text{m}^2$ whereas samples B1–B4 have $W = 2\mu\text{m}$ which gives an interface area of $5\mu\text{m}^2$ and thus there is a bias in the interface areas.

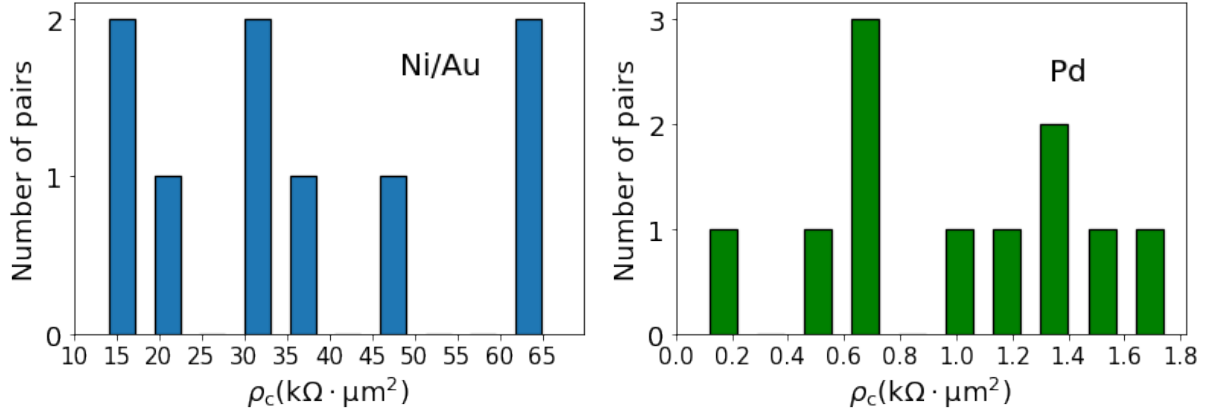


Figure 3.10: **Contact resistivity of Pd and Ni/Au.** Horizontal axis shows the contact resistivity and vertical axis shows the number of contact pairs. Ni/Au contact resistances were obtained from 9 different pairs of contacts with an interface area of $31.25\mu\text{m}^2$. Pd contact resistances were obtained from 11 different pairs of contacts with an interface area of $5\mu\text{m}^2$.

Chapter 4

Current annealing of graphene

Being a 2D material, graphene is extremely sensitive to surface contamination, and thus, removing the presence of impurities is an important factor in graphene based electronic devices since they may affect the electronic transport properties. One of the typical impurities comes from the residue of resist used in the lithography. In our graphene Hall bars, standard solvent strippers such as acetone did not remove the residual resist present on the sample after the process, and a different approach was needed. Common approaches taken to remove dopants on graphene devices include annealing under a vacuum condition [44, 66, 67] or in argon(Ar)/hydrogen(H₂) forming gas [11, 51, 58, 68] at several hundreds of degrees. Ishigami *et al.* reported the residual photoresist removal in Ar/H₂ atmosphere at 400C°. Annealing time is 1 hour, with gas flow rates of 1,700 mL/min (Ar) and 1,900 mL/min (H₂) [51]. Alexandrou *et al.* describe that water and oxygen molecules in the surrounding environment play a large role in p-doping graphene by demonstrating a significant shift in Dirac point over a period of air exposure to their graphene field effect transistors (FETs) [66]. Graphene FETs are commonly fabricated by encapsulating graphene with other materials such as parylene-C/aluminum [66, 69] and by inserting an amorphous fluoropolymer film in between graphene and the SiO₂ substrate [70] to prevent graphene from being doped by the air exposure. Alexandrou *et al.* shows the effect of thermal annealing on their graphene FETs under vacuum at and $T = 390\text{K}$ and $T = 450\text{K}$ for different duration.

Another common method to remove dopants on graphene surface is to apply a high biasing electrical current through it to create a large current density, which leads to a high heat dissipation over the graphene surface. Graphene can sustain a high current without being damaged, and the particles on graphene may be melted, evaporated, or sublimated by the high temperature induced by the Joule heating [71]. This annealing method is preferred

especially for low-temperature measurements, since it can be performed in the cryostat without air exposure of graphene prior to the measurement. Giesbers *et al.* demonstrated the *in situ* current annealing of their exfoliated graphene Hall bar sample at $T = 380\text{K}$ for several hours before cooling down the sample which brought the Dirac point to $V_g = 5\text{V}$ and a mobility to $8,000\text{ cm}^2\text{ V}^{-1}\text{s}^{-1}$ [41]. Geisenhof *et al.* uses the current annealing procedure for multiple cycles at 1.6K , while DC resistance (R_{DC}) is monitored. R_{DC} decreases as DC bias voltage is increased, and starts to increase again when the current is saturated. The maximum current density of $0.35\text{mA}\mu\text{m}^{-1}$ was reached [35]. Moser *et al.* performs the current annealing at $T = 76\text{K}$. Their sample consists of a $W = 4\mu\text{m}$ and $L = 1\mu\text{m}$ monolayer graphene contacted by Cr/Au electrodes on SiO_2/Si substrate. A source-drain bias voltage of a few volts is applied, which causes a high current density of a few $10^8\text{A}/\text{cm}^2$ in graphene, which then induces a significant increase in sample temperature. This effect is referred to as the Joule heating. The estimated temperature reached on their graphene devices is $\sim 600\text{C}^\circ$. They confirm the effect of their annealing by depositing cadmium selenide particles on graphene and observing the difference in atomic force microscopy (AFM) measurements before and after annealing. In addition to the AFM measurements, they perform the two-point measurement of conductance vs back-gate voltage (V_{bg}) from -20V to 20V , and show that the conductance minimum is near $V_{\text{bg}} = 0\text{V}$ after annealing whereas it is higher than 20V before the current annealing [71].

This method demonstrated by Moser *et al.* is referenced in our method of current annealing. At $V_{\text{bg}} = 0\text{V}$, the bias voltage is slowly raised and held constant while monitoring the time dependence of the current I . The bias voltage is further increased if I stays constant, and is kept being increased until it starts to continuously decay over time. The annealing current density J is determined by the current I per cross-sectional area A which current goes through, i.e. $J = I/A = I/(t \times W)$ where the thickness of graphene t is $t \sim 0.345\text{ nm}$ and W is the width of the Hall bar. Fig.4.1 shows the typical annealing current curve as a function of time. The bias voltage is increased until annealing current reaches 0.87mA . At a fixed bias voltage, current starts to decay, and saturates after 40 minutes. Typically, our samples are annealed for 20 minutes which is when the current generally shows a saturation or a decay that is slowed down. The bias voltage V was generated and then converted to current by the Keithley 2401 SourceMeter for $V \leq 20\text{V}$, and the same method was taken using the Keithley 230 Programmable Voltage Source for $V > 20\text{V}$. The annealing current is then applied through a pair of contacts.

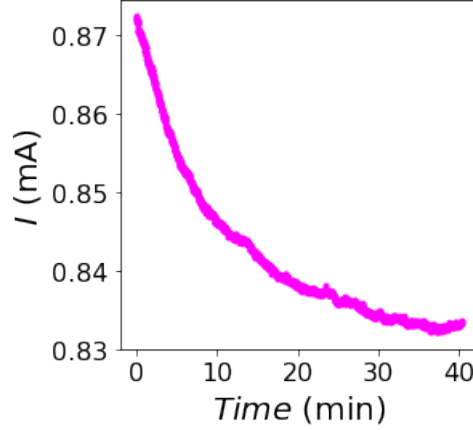


Figure 4.1: **Annealing current as a function of time.**

4.1 Dirac point shift

4.1.1 Doping of graphene

This section will discuss some of the characterization done on the samples before and after current annealing, and how annealing modified the doping in each sample. Two-terminal measurement of current across contact 1-6 at RT on sample A3 shows $V_D = 9.9V$, and applying an annealing current through the same pair of contact at $I = 0.9mA$ for 20 minutes at RT shifted the Dirac point to $V_D = 8.6V$ at RT which was found by performing the same two-terminal measurement. Sample A3 was then annealed again at RT through the same pair of contact with current $I = 1.55mA$ for 20 minutes. Two-terminal measurement of current exhibited a relatively flat dip around $V_{bg} \sim 0V$ which suggest a presence of multiple Dirac points. We then annealed the sample through a few different pairs of Ohmic contacts at RT to anneal the whole graphene channel. First, annealing current at $I = 1.55mA$ was applied through contacts 4 – 5 with a bias voltage of 39V for 20 minutes. Next, annealing current at $I = 1.52mA$ was applied through contacts 2 – 7 for 20 minutes with a bias voltage of 14V. Lastly, annealing current at $I = 1.51mA$ was applied through contacts 3 – 8 for 20 minutes with a bias voltage of 14V. All of the annealing was performed at RT. The two-terminal measurement of current at RT through the contact pair 4 – 5 after all of the above annealing exhibited a dip at $V_{bg} = 0V$ and another smaller dip at $V_{bg} = -24.5V$. The highest mobility obtained from this sample is $2,487 \text{ cm}^2V^{-1}s^{-1}$ at $V_{bg} = 0V$ with a density of $8.62 \times 10^{11}/\text{cm}^2$ before annealing, and $3,243 \text{ cm}^2V^{-1}s^{-1}$ at $V_{bg} = 20V$ with

a density of $9.77 \times 10^{11}/\text{cm}^2$ after annealing. Fig.4.2 shows the typical resistance curve of graphene measured at RT and at $T = 1.64\text{K}$ before and after annealing. Compared to before annealing, the curves become broader and more asymmetric after annealing for both RT and $T = 1.64\text{K}$. Annealing is generally effective in shifting the Dirac point towards $V_{\text{bg}} = 0\text{V}$ by $1\sim 2\text{V}$ which imply that sources of charged impurities such as absorbed molecules are removed through annealing, but the transport characterization of samples after annealing reveals that our method of current annealing leads to a higher disorder in graphene. The highest mobility obtained in this sample is $1,754 \text{ cm}^2\text{V}^{-1}\text{s}^{-1}$ at $V_{\text{bg}} = -5\text{V}$ with a density of $9.8 \times 10^{11}/\text{cm}^2$ before annealing, and $3,327 \text{ cm}^2\text{V}^{-1}\text{s}^{-1}$ at $V_{\text{bg}} = 20\text{V}$ with a density of $13.41 \times 10^{11}/\text{cm}^2$ after annealing. A possible reason of increased mobility due to annealing despite the enhanced graphene disorder is the lowered resistance in graphene after annealing at the Dirac point which most likely is a result of removed impurities on graphene. The measurement is taken on the sample A1.

Fig.4.3 shows the change in resistance of graphene before and after annealing at several different current values. Resistance was measured after each annealing at room temperature. Clear change in the doping of graphene is observed as higher annealing current is applied. The resistance curves in green and purple have two distinct peaks corresponding to two Dirac points, showing a strong disorder in graphene. For example, multiple Dirac points are observed in the study done by Song *et al.* in which they demonstrate proximity effect in graphene- Cd_3As_2 heterostructures. Cd_3As_2 is also a semi-metal and is a 3D Dirac material. At the graphene- Cd_3As_2 interface, electrons are transferred from Cd_3As_2 to graphene due to the difference in work function between the two materials, and this induces a n -type doping in graphene. Cd_3As_2 nanoplates are stacked on monolayer graphene and the graphene is contacted by Pd/Au electrodes in a way that graphene is partially covered by the nanoplates and the two regions are in series. As expected, their measured total resistance of the sample as a function of back-gate voltage V_{g} clearly shows two CNPs: one for exposed graphene at $V_{\text{g}} = 11.4\text{V}$ and another for Cd_3As_2 -covered graphene at $V_{\text{g}} = -12.8\text{V}$ [72]. Note that the materials on their sample are not only graphene and thus modification in electronic structure and transport properties are expected. Determining the sources of disorder brought by the annealing may require an understanding of the physics of graphene surface at microscopic level which can be performed by techniques such as scanning tunnelling microscopy (STM) to probe the electronic disorder in graphene and study the spatial variation in the density. An example study is done by Zhang *et al.* where topography of graphene surface and the corresponding spatial profile of charge puddle in graphene are characterized [53].

The highest mobility obtained from the measured sample is $1,326 \text{ cm}^2\text{V}^{-1}\text{s}^{-1}$ at $V_{\text{bg}} = -10\text{V}$ with a density of $16.6 \times 10^{11}/\text{cm}^2$ before annealing, and no mobility measurement was

taken after annealing. Data is taken from sample B1. The general trend of resistance curve measured on our graphene samples before and after annealing is that resistance values at the Dirac point are reduced and the peaks become wider after annealing once certain value of current density is reached. It is also challenging to shift the Dirac point by a significant amount while maintaining the homogeneity of graphene prior to any annealing processes. We succeeded in increasing the mobility of graphene by annealing the samples, but mobility was also reduced in a few samples due to annealing, and similar results are observed in [73]. Establishing and demonstrating a method of annealing is thus a part of future goal of this research.

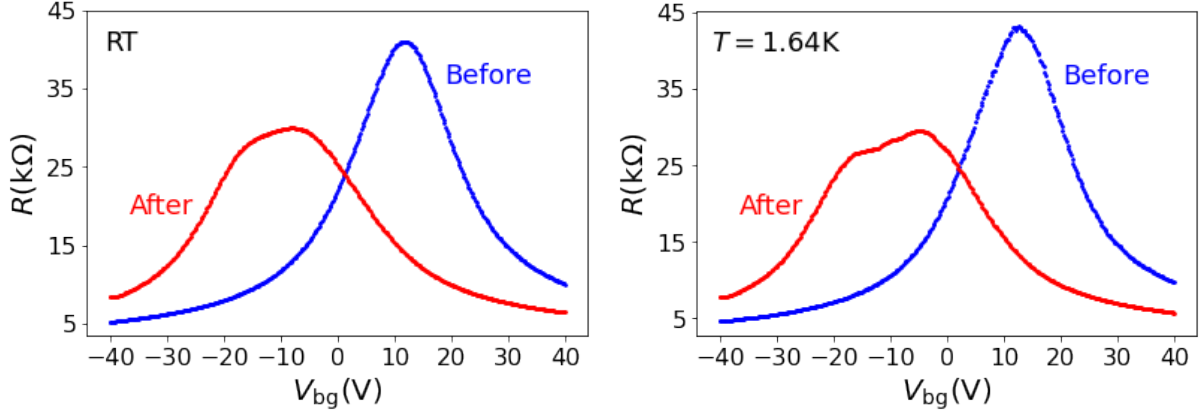


Figure 4.2: **Resistance of graphene measured at RT and 1.64K before and after annealing on sample A1.** Resistance of graphene measured at room temperature (left figure) and at $T = 1.64\text{K}$ (right figure) before (blue) and after (red) annealing. Annealing was performed at room temperature for ~ 20 minutes. Annealing current was at $I = 1.43\text{mA}$ which provided a current density of $8.3 \times 10^7 \text{A/cm}^2$, and decayed to $I = 1.1\text{mA}$ after 20 minutes. Annealing current was generated by applying a bias voltage of 37V . Dirac point is at $V_D = 11.8\text{V}$ at RT and at $V_D = 12.6\text{V}$ at $T = 1.64\text{K}$ before annealing. Measurements are taken from sample A1 with four-terminal constant AC excitation current at $I = 100\text{nA}$.

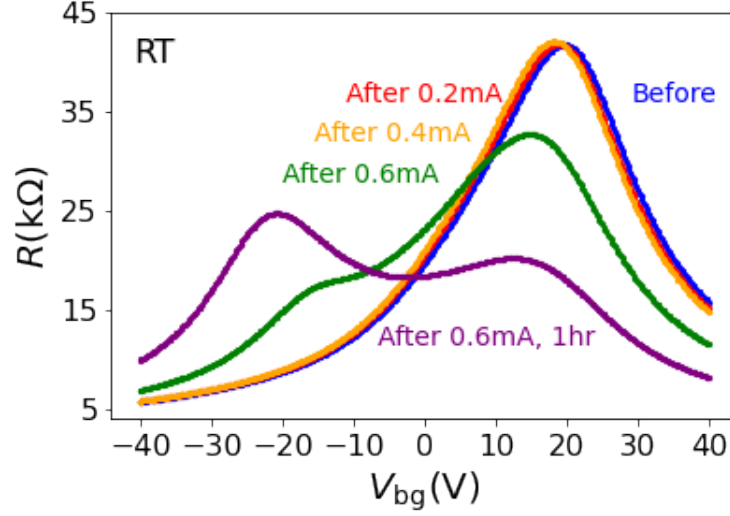


Figure 4.3: **Change in the resistance of graphene measured at RT before and after annealing.** Change in the resistance of graphene measured at room temperature before and after annealing at several different current densities. Graphene was annealed at $I = 0.2\text{mA}$, $I = 0.4\text{mA}$, and at $I = 0.6\text{mA}$. Annealing was performed once at $I = 0.2\text{mA}$ and $I = 0.4\text{mA}$, and performed twice at $I = 0.6\text{mA}$ for 20 minutes and 60 minutes. Duration of annealing was 20 minutes for the first three annealing processes, and 60 minutes for the last annealing process. Corresponding current density is $2.9 \times 10^7 \sim 8.7 \times 10^7 \text{A/cm}^2$. The Dirac points locations are $V_D = 19.6\text{V}$ before annealing, $V_D = 18.8\text{V}$ after annealing at $I = 0.2\text{mA}$, $V_D = 18.2\text{V}$ after annealing at $I = 0.4\text{mA}$, $V_D = 14.8\text{V}$ and $V_D = -15\text{V}$ after annealing at $I = 0.6\text{mA}$, and $V_D = -20.8\text{V}$ and $V_D = 14.2\text{V}$ after annealing at $I = 0.6\text{mA}$ for 60 minutes. Measurements are taken from sample B1.

Chapter 5

Conclusions

The electronic transport properties of single-layer graphene grown by chemical vapor deposition (CVD) are characterized under magnetic field and cryogenic temperature. Graphene is a 2-dimensional material of carbons arranged in a honeycomb lattice with its physics governed by the Dirac fermions. Its extraordinary conductivity and the tunable electronic properties make graphene highly potential as a next-generation material in nano-electronic devices. Recently discovered superconductivity in graphene also inspires applications in quantum information science. The graphene growth with CVD has significantly progressed and provides a possible route to a scalable fabrication of high-performance graphene devices. However, CVD graphene still suffers from its relatively lower carrier mobility than exfoliated graphene due to the conventional wet-transfer done after the graphene growth.

In this thesis, the basic theory of electronic structure in graphene is discussed in Chapter 1, and some of the novel physics of graphene that originates in its unique electronic structure are demonstrated in Chapter 3 and 4. The electric field effect and the Dirac point in graphene are clearly observed by applying an external gate voltage, and the results agree with the gate voltage dependence in mobility. The characterized graphene samples contain microscopic disorders originating from the graphene growth in CVD, fabrication processes, and the exposure of samples in the ambient conditions. We studied the effect of current annealing on our graphene samples. Mobility was increased in some of the samples and shift in the Dirac point was observed implying that annealing was effective in removing some charged impurities on the samples. The resistance in Ni/Au and Pd Ohmic contacts was studied and compared, and the data shows significantly smaller resistance in Pd contacts.

Quantum Hall effect (QHE) is an evidence of 2-dimensional nature and the QHE in graphene is known to occur at half-integer values in contrast to the integer QHE observed in

conventional 2DEGs. The characterization of QHE was not achieved in the study presented in this thesis, and we observed in the magnetoresistance the quadratic dependence in the magnetic field. This agrees with the magnetoresistance observed in a few-layer graphene, that is a normal metal, instead of a single-layer graphene. This result also implies the low quality of our samples and the mobility of graphene which is limited by the sources of disorder. Many challenges in the large-scale fabrication of graphene devices were learned, and the work presented here provides a foundation to the research on graphene quantum nano-electronic devices studied in our group.

The performance of graphene devices is known to largely depend on the quality of graphene surface and its interface with substrates in the heterostructure. The experimental study on graphene presented here emphasized the importance of the understanding of graphene physics in a microscopic level. Thus, imaging and spectroscopy techniques can be further utilized to study the CVD grown graphene. There are possible improvements in the fabrication of CVD graphene Hall bars that have not been explored. Photolithography provides a cost-efficient fabrication, but it has been reported that residual photoresists significantly p-dopes graphene, and that is shown in our results. Photoresists are also known to be hardened by the O_2 plasma etching process, and its residue was a critical source that limits the yield of our Hall bar devices.

References

- [1] L.E.F.Foa Torres, Stephan Roche, and Jean-Christophe Charlier. *Introduction to Graphene-Based Nanomaterials: From Electronic Structure to Quantum Transport*. Cambridge University Press, 2014.
- [2] H.-S.Philip Wong and Deji Akinwande. *Carbon Nanotube and Graphene Device Physics*. Cambridge University Press, 2010.
- [3] N.M.R.Peres. “Colloquium: The transport properties of graphene: An introduction”. In: *Rev.Mod.Phys.* 82.2673 (2010).
- [4] Z.Jiang et al. “Infrared Spectroscopy of Landau Levels of Graphene”. In: *Phys.Rev.Lett.* 98.197403 (2007).
- [5] K.S.Novoselov et al. “Two-dimensional gas of massless Dirac fermions in graphene”. In: *Nature* 438.197–200 (2005).
- [6] S.V.Morozov et al. “Strong Suppression of Weak Localization in Graphene”. In: *Phys.Rev.Lett.* 97.016801 (2006).
- [7] I.Gierz, C.Riedl, U.Starke, C.R.Ast, and K.Kern. “Atomic hole doping of graphene.” In: *Nano Lett.* 8.4603 (2008).
- [8] S.M.Sze and Kwok K.Ng. *Physics of Semiconductor Devices*. John Wiley & Sons, 2006.
- [9] K.S.Novoselov et al. “Electric Field Effect in Atomically Thin Carbon Films”. In: *Science* 306.666 (2004).
- [10] L.Banszerus et al. “Ultrahigh-mobility graphene devices from chemical vapor deposition on reusable copper”. In: *Sci.Adv.* 1.6 (2015).
- [11] D.De Fazio et al. “High-Mobility, Wet-Transferred Graphene Grown by Chemical Vapor Deposition”. In: *ACS Nano* 13.8 (2019).
- [12] J.-H.Lee et al. “Wafer-Scale Growth of Single-Crystal Monolayer Graphene on Reusable Hydrogen-Terminated Germanium”. In: *Science* 344.6181 (2014).

- [13] S.Lee, K.Lee, and Z.Zhong. “Wafer Scale Homogeneous Bilayer Graphene Films by Chemical Vapor Deposition”. In: *Science* 10.4702–4707 (2010).
- [14] S. Mikhailov. *Physics and Applications of Graphene - Experiments*. InTech, 2011.
- [15] M.Wang et al. “A Platform for Large-Scale Graphene Electronics – CVD Growth of Single-Layer Graphene on CVD-Grown Hexagonal Boron Nitride”. In: *Adv.Mater.* 25.2746–2752 (2013).
- [16] A.Pirkle et al. “The effect of chemical residues on the physical and electrical properties of chemical vapor deposited graphene transferred to SiO₂”. In: *Appl.Phys.Lett.* 99.122108 (2011).
- [17] L.Huang et al. “Graphene/Si CMOS hybrid Hall integrated circuits”. In: *Sci.Rep.* 4.5548 (2014).
- [18] J.Dauber et al. “Ultra-sensitive Hall sensors based on graphene encapsulated in hexagonal boron nitride”. In: *Appl.Phys.Lett.* 106.193501 (2015).
- [19] Y.M.Lin et al. “100-GHz transistors from wafer-scale epitaxial graphene”. In: *Science* 327.662 (2010).
- [20] X.Gan et al. “Graphite-N Doped Graphene Quantum Dots as Semiconductor Additive in Perovskite Solar Cells”. In: *ACS Appl.Mater.Interfaces* 11.41 (2019).
- [21] W.S.Hwang et al. “Graphene nanoribbon field-effect transistors on wafer-scale epitaxial graphene on SiC substrates”. In: *APL Materials* 3.011101 (2015).
- [22] Y.Cao et al. “Unconventional superconductivity in magic-angle graphene superlattices”. In: *Nature* 556.43–50 (2018).
- [23] D.Rodan-Legrain et al. “Highly tunable junctions and non-local Josephson effect in magic-angle graphene tunnelling devices”. In: *Nat.Nanotechnol.* 16.769–775 (2018).
- [24] D.K.Efetov et al. “Specular interband Andreev reflections at van der Waals interfaces between graphene and NbSe₂”. In: *Nature Phys* 12.328–332 (2016).
- [25] D.Wang et al. “Andreev Reflections in NbN/Graphene Junctions under Large Magnetic Fields”. In: *Nano Lett.* 21.82298235 (2021).
- [26] Y.Shimazaki et al. “Generation and detection of pure valley current by electrically induced Berry curvature in bilayer graphene”. In: *Nature Phys* 11.1032–1036 (2015).
- [27] V.Gall, R.Kraft, I.V.Gornyi, and R.Danneau. “Spin and valley degrees of freedom in a bilayer graphene quantum point contact: Zeeman splitting and interaction effects”. In: *Phys.Rev.Research* 4.023142 (2022).

- [28] D.Xiao, W.Yao, and Q.Niu. “Valley-Contrasting Physics in Graphene: Magnetic Moment and Topological Transport”. In: *Phys.Rev.Lett.* 99.236809 (2007).
- [29] R.V.Gorbachev et al. “Detecting topological currents in graphene superlattices”. In: *Science* 346.448–451 (2014).
- [30] K.Komatsu et al. “Observation of the quantum valley Hall state in ballistic graphene superlattices”. In: *Sci.Adv.* 4.5 (2018).
- [31] K.v. Klitzing, G. Dorda, and M. Pepper. “New method for high accuracy determination of the fine-structure constant based on quantized Hall resistance”. In: *Phys. Rev. Lett.* 45.6 (1980).
- [32] Y.Zhang, Y.W.Tan, H.L.Stormer, and P.Kim. “Experimental observation of the quantum Hall effect and Berry’s phase in graphene”. In: *Nature* 438.201 (2005).
- [33] K.S.Novoselov et al. “Room-Temperature Quantum Hall Effect in Graphene”. In: *Science* 315.5817 (2005).
- [34] Z.Tan et al. “Shubnikov-de Haas oscillations of a single layer graphene under dc current bias”. In: *Phys.Rev.B* 84.115429 (2011).
- [35] F.R.Geisenhof et al. “Quantum anomalous Hall octet driven by orbital magnetism in bilayer graphene”. In: *Nature* 598.53–58 (2021).
- [36] M.Serlin et al. “Intrinsic quantized anomalous Hall effect in a moiré heterostructure”. In: *arXiv* 1907.00261 (2019).
- [37] Y.Cao et al. “Correlated insulator behaviour at half-filling in magic-angle graphene superlattices”. In: *RSC Adv.* 80.556 (2018).
- [38] Y.Zhang, D.Mao, Y.Cao, P.Jarillo-Herrero, and T. Senthil. “Nearly flat Chern bands in moiré superlattices”. In: *Phys.Rev.B* 99.075127 (2019).
- [39] B.Lian, X.Q.Sun, A.Vaezi, X.L.Qi, and S.C.Zhang. “Topological quantum computation based on chiral Majorana fermions”. In: *Proceedings of the National Academy of Sciences* 115.43 (2018).
- [40] T.J.B.M.Janssen, A.Tzalenchuk, S.Lara-Avila, S.Kubatkin, and V.I.Fal’ko. “Quantum resistance metrology using graphene”. In: *Rep.Prog.Phys.* 76.104501 (2013).
- [41] A.J.M.Giesbers et al. “Quantum resistance metrology in graphene”. In: *Appl.Phys.Lett.* 93.222109 (2008).
- [42] A.Tzalenchuk1 et al. “Towards a quantum resistance standard based on epitaxial graphene”. In: *Nature Nanotech* 5.186–189 (2010).

- [43] F.Delahaye¹ and B.Jeckelmann. “Revised technical guidelines for reliable dc measurements of the quantized Hall resistance.” In: *Metrologia* 40.217 (2003).
- [44] R.Ribeiro-Palau et al. “Quantum Hall resistance standard in graphene devices under relaxed experimental conditions”. In: *Nature Nanotech* 10.965–971 (2015).
- [45] C.R.Dean et al. “Boron nitride substrates for high-quality graphene electronics”. In: *Nature Nanotech* 5.722–726 (2010).
- [46] J.Wang, F.Ma, and M.Sun. “Graphene, hexagonal boron nitride, and their heterostructures: properties and applications”. In: *RSC Adv.* 7.16801 (2017).
- [47] C.R.Dean et al. “Multicomponent fractional quantum Hall effect in graphene”. In: *Nature Phys* 7.693–696 (2011).
- [48] K.Gopinadhan et al. “Extremely large magnetoresistance in few-layer graphene/boron–nitride heterostructures”. In: *Nat Commun* 6.8337 (2015).
- [49] B. Fülöp et al. “Boosting proximity spin–orbit coupling in graphene/WSe₂ heterostructures via hydrostatic pressure”. In: *npj 2D Materials and Applications* 5.82 (2021).
- [50] Z.Wang et al. “Strong interface-induced spin–orbit interaction in graphene on WS₂”. In: *Nat Commun* 6.8339 (2015).
- [51] M.Ishigami et al. “Atomic Structure of Graphene on SiO₂”. In: *Nano Lett.* 7.1643 (2007).
- [52] J.Martin et al. “Observation of electron–hole puddles in graphene using a scanning single-electron transistor”. In: *Nature Phys* 4.144–148 (2008).
- [53] Y.Zhang, V.W.Brar, C.Girit, A.Zettl, and M.F.Crommie. “Origin of spatial charge inhomogeneity in graphene”. In: *Nature Phys* 5.722–726 (2009).
- [54] S.Sarkar et al. “Role of different scattering mechanisms on the temperature dependence of transport in graphene”. In: *Sci Rep* 5.16772 (2015).
- [55] H.-Z.Lu and S.-Q.Shen. “Weak localization and weak anti-localization in topological insulators”. In: *arXiv* 1409.1299 (2014).
- [56] Y.Liu, W.S.Lew, and L.Sun. “Enhanced weak localization effect in few-layer graphene”. In: *Phys.Chem.Chem.Phys.* 13.20208–20214 (2011).
- [57] J.Billy et al. “Direct observation of Anderson localization of matter waves in a controlled disorder”. In: *Nature* 453.891–894 (2008).

- [58] T.Iwasaki et al. “Bubble-Free Transfer Technique for High-Quality Graphene/Hexagonal Boron Nitride van der Waals Heterostructures”. In: *ACS Applied Materials & Interfaces* 12.7 (2020).
- [59] S.Tanabe, Y.Sekine, H.Kageshima, M.Nagase, and H.Hibino. “Half-Integer Quantum Hall Effect in Gate-Controlled Epitaxial Graphene Devices”. In: *Appl.Phys.Express* 3.075102 (2010).
- [60] T.Cusati et al. “Electrical properties of graphene-metal contacts”. In: *Sci Rep* 7.5109 (2017).
- [61] T.J.B.M.Janssen et al. “Precision comparison of the quantum Hall effect in graphene and gallium arseniden”. In: *Metrologia* 49.294 (2012).
- [62] K.Nagashio, T.Nishimura, K.Kita, and A.Toriumi. “Metal/Graphene Contact as a Performance Killer of Ultra-high Mobility Graphene - Analysis of Intrinsic Mobility and Contact Resistance -”. In: *2009 IEEE International Electron Devices Meeting* (2009), pp. 1–4.
- [63] K.Nagashio, T.Nishimura, K.Kita, and A.Toriumi. “Contact Resistivity and Current Flow Path at Metal/graphene Contact”. In: *Appl.Phys.Lett.* 97.143514 (2010).
- [64] B.Huard, N.Stander, J.A.Sulpizio, and D.Goldhaber-Gordon. “Evidence of the Role of Contacts on the Observed Electron-hole Asymmetry in Graphene”. In: *Phys.Rev.B* 78.121402(R) (2008).
- [65] S.M.Song, J.K.Park, O.J.Sul, and B.J.Cho. “Determination of Work Function of Graphene under a Metal Electrode and Its Role in Contact Resistance”. In: *Nano Lett.* 12.8 (2012).
- [66] K. Alexandrou et al. “Effect of vacuum thermal annealing to encapsulated graphene field effect transistors”. In: *Journal of Vacuum Science & Technology B* 34.041805 (2016).
- [67] M.-S.Choi et al. “High carrier mobility in graphene doped using a monolayer of tungsten oxyarsenide”. In: *Nat Electron* 4.731–739 (2021).
- [68] M.Yankowitz et al. “Emergence of superlattice Dirac points in graphene on hexagonal boron nitride”. In: *Nature Phys* 8.382–386 (2012).
- [69] P.-H.Ho et al. “Self-Encapsulated Doping of n-Type Graphene Transistors with Extended Air Stability”. In: *ACS Nano* 6.6215 (2012).
- [70] W.C.Shin, S.Seo, and B.J.Cho. “Highly air-stable electrical performance of graphene field effect transistors by interface engineering with amorphous fluoropolymer”. In: *Appl.Phys.Lett.* 98.153505 (2011).

- [71] J.Moser, A.Barreiro, and A. Bachtold. “Current-induced cleaning of graphene”. In: *Appl.Phys.Lett.* 91.163513 (2007).
- [72] H.-D.Song et al. “Asymmetric magneto-transport in a Dirac semimetal heterostructure”. In: *Appl.Phys.Lett.* 114.243107 (2019).
- [73] S.Tanaka et al. “Effect of current annealing on electronic properties of multilayer graphene”. In: *J.Phys.:Conf.Ser.* 232.012015 (2010).
- [74] R.Shi, H.Xu, B.Chen, Z.Zhang, and L.Peng. “Scalable fabrication of graphene devices through photolithography”. In: *Appl.Phys.Lett.* 102.113102 (2013).

APPENDICES

Appendix A

Device Fabrication

A.1 Fabrication recipes

Fabrication of graphene Hall bars were performed using the equipment in the Quantum-Nano Fabrication and Characterization Facility (QNFCF). The detailed recipes and the equipment used for fabrication are described below for each process.

1. Photolithography

■ Alignment marks and electrodes

(a) Spin-coating MMA (8.5) (QNFCF – Brewer E-beam spinner)

- Spin recipe:
 - i. 5000 rpm, 500 rpm/s, 60 sec
 - ii. 0 rpm, 500 rpm/s, 10 sec
- Bake: 180 C° for 5 min

(b) Spin-coating Shipley 1805 (QNFCF – Brewer UV spinner)

- Spin recipe:
 - i. 500 rpm, 500 rpm/s, 1 sec
 - ii. 5000 rpm, 1000 rpm/s, 30 sec
 - iii. 0 rpm, 1000 rpm/s, 10 sec
- Bake: 120C° for 90 sec

(c) Shipley 1805 exposure (QNFCF – MLA150)

- Dose 95 mJ/cm², Defocus 2
- (d) Shipley 1805 development (QNFCF – UV develop bench)
 - i. MF-319 for 1 min
 - ii. DI water
- (e) MMA (8.5) exposure (QNFCF – Novascan UV ozone)
 - i. Pre-bake for 150C° for 5 min on a hotplate
 - ii. 25C° for 15 min, 9cm stage height
- (f) MMA (8.5) development (QNFCF – Solvent bench)
 - i. IPA:DI / 35ml:15ml for 2 min 40 sec
 - ii. DI water

■ Hall bars

- (a) Spin-coating MMA (8.5) (QNFCF – Brewer E-beam spinner)
 - Spin recipe:
 - i. 5000 rpm, 500 rpm/s, 60 sec
 - ii. 0 rpm, 500 rpm/s, 10 sec
 - Bake: 180 C° for 5 min
- (b) Spin-coating Shipley 1811 (QNFCF – Brewer UV spinner)
 - Spin recipe:
 - i. 500 rpm, 500 rpm/s, 1 sec
 - ii. 5000 rpm, 1000 rpm/s, 30 sec
 - iii. 0 rpm, 1000 rpm/s, 10 sec
 - Bake: 120C° for 90 sec
- (c) Shipley 1811 exposure (QNFCF – MLA150)
 - Inversion
 - Dose 85 mJ/cm², Defocus 0
- (d) Shipley 1811 development (QNFCF – UV develop bench)
 - i. MF-319 for 90 sec
 - ii. DI water
- (e) MMA (8.5) exposure (QNFCF – Novascan UV ozone)
 - i. Pre-bake for 150C° for 5 min on a hotplate
 - ii. 25C° for 15 min, 9 cm stage height
- (f) MMA (8.5) development (QNFCF – Solvent bench)

- i. IPA:DI / 35 ml:15 ml for 2 min 40 sec
- ii. DI water

2. Etching (QNFCF – YES plasma strip)

- RF power: 200 W
- Pressure: 300 mTorr
- Temperature: 25C°
- O₂ flow: 40 sccm
- Duration: 1 min (alignment marks) or 10 min (Hall bars)

3. Metalization

■ Deposition (QNFCF – Angstrom E-beam evaporator)

- Alignment marks
 - (a) Titanium/Gold
 - Thickness: 20/80 nm
 - Deposition rate: 3A/s for both
- Electrodes
 - (a) Nickel/Gold
 - Thickness: 20/80 nm
 - Deposition rate: 2A/s (Ni) and 3A/s (Au)
 - (b) Palladium
 - Thickness: 50 nm
 - Deposition rate: 3A/s

■ Liftoff

- i Remover PG¹
- ii Acetone
- iii IPA

4. Resist removal

- i Acetone²

¹Soaking the sample in Remover PG for ~2 days was found to be the most optimal to avoid the use of liftoff tools such as pipettes, which potentially damage graphene.

²Gently move the sample after putting it in a beaker.

- ii Remover PG for ~ 10 sec³
 - iii Isopropyl alcohol (IPA)⁴
5. Pre-process and post-process baking (QNFCF – Fisher oven)
- Gas: N₂
 - Temperature: 180C°
 - Duration: 30 min

It is preferred to complete each of step 1~3 of processes listed in the section 2.2 to minimize the duration of time for chemicals to be in contact with graphene. We have noticed that graphene is damaged in every fabrication run after the first spin-coating of methyl methacrylate (MMA). To address this issue, we added the baking process as described in 1(a), 2(a), and 3(a) to remove liquid present underneath the graphene layer. Additionally, we used a spin-coating recipe of MMA (first resist to coat) with a low acceleration so that the friction from spin-coating will not tear off the graphene. Before spin-coating photoresist, MMA is coated as the first layer of resist on graphene to avoid any photoresist to directly contact graphene. Photoresist contaminates graphene and can significantly degrade its quality by doping or creating scattering centers [74]. Poly methyl methacrylate (PMMA) is a similar compound to MMA, which is commonly used as a resist for EBL processes.

We attempted to metallize graphene (section 2.2 step 3) before patterning graphene channels (section 2.2 step 2) to achieve a clean contact of electrodes on graphene, but a metal layer did not adhere properly on graphene because of the weak van der Waals attraction in between metal and graphene. Thus, metalization must be performed directly on SiO₂ for a proper adhesion.

We observed noticeably large amount of residual resist on the sample as shown in Fig.A.1 around some of the Hall bars after fabrication step 2(d) described in section 2.2. This residue is most likely the photoresist hardened by the O₂ plasma etching process, and acetone does not remove this type of resists. This residue tends to remain on graphene, and it significantly lowered the yield of fabrication. Thus, it remains as a future task to avoid this resist residue on the sample. Using Remover PG as a resist remover did not leave residue on the samples. However, some reports point out the low compatibility of

³Remover PG is a N-Methyl-2-pyrrolidone (NMP)-based solvent stripper. The purpose here is to minimize the residual resist on the sample.

⁴Rinse in two IPA solutions.

NMP-based photoresist stripper with graphene, and thus we tried to minimize its use. Fig.A.2 shows the graphene Hall bar after fabrication processes without baking the sample in the oven before resist spin-coating. Significant damage can be seen on graphene. Most of this damage is likely to be caused by the resist spin-coating. Metal liftoff may have torn off some graphene.

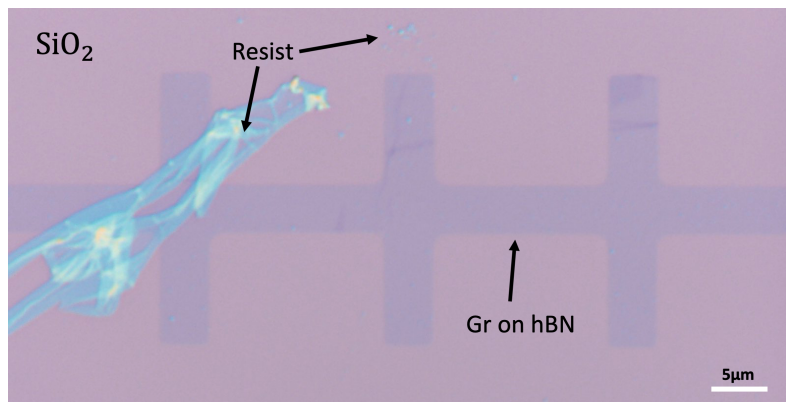


Figure A.1: **Optical micrograph of graphene channel after step 2(d) of section 2.2.**

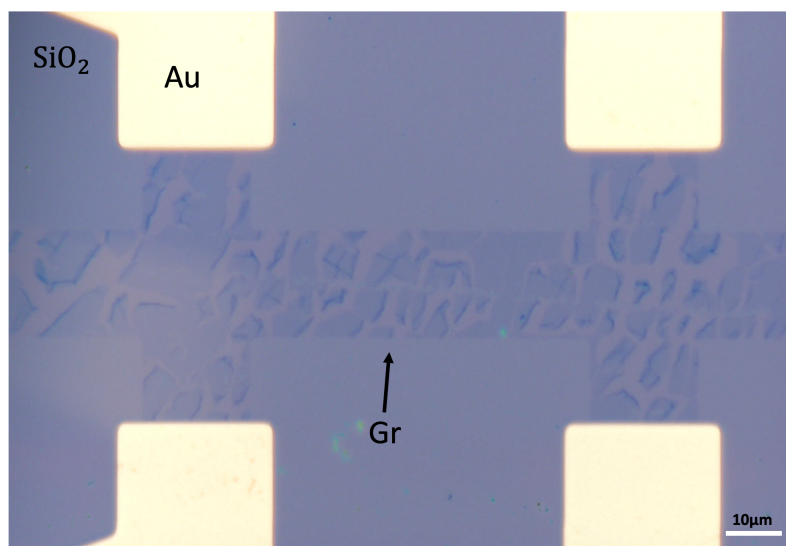


Figure A.2: **Optical micrograph of graphene Hall bar without pre-baking. A section of Hall bar showing damaged graphene.**

Use of heat and sonication was avoided when graphene was exposed to solvents such as Remover PG. We found that these tools can cause a drastic damage to graphene.

Etching of graphene has also been performed with RIE. The recipe is described below.

■ Oxford Instruments ICP380

- RF power: 20 W
- O₂/Ar flow: 10/30 sccm
- Pressure: 80 mTorr
- Duration: 1 min